Article

Structural Properties of HEHN- and HAN-Based Ionic Liquid Mixtures: A Polarizable Molecular Dynamics Study

Shehan M. Parmar, Daniel D. Depew, Richard E. Wirz, and Ghanshyam L. Vaghjiani*

Read Online
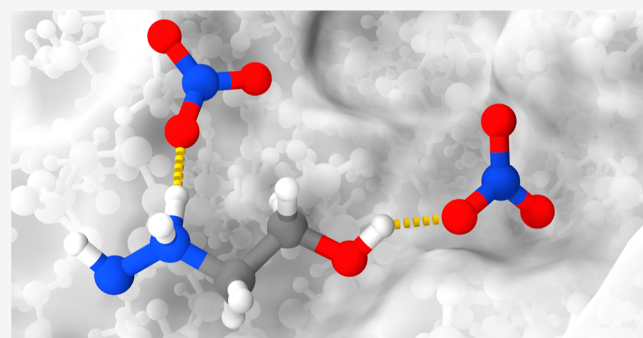
ACCESS | 📊 Metrics & More | 📖 Article Recommendations | 🆂🅸 Supporting Information

ABSTRACT: Molecular dynamics simulations of binary mixtures comprising 2-hydroxyethylhydrazinium nitrate (HEHN) and hydroxylammonium nitrate (HAN) were conducted using the polarizable APPLE&P force field to investigate fundamental properties of multimode propulsion (MMP) propellants. Calculated densities as a function of temperature were in good agreement with experiments and similar simulations. The structural properties of neat HEHN and HAN−HEHN provided insights into their inherent, protic nature. Radial distribution functions (RDFs) identified key hydrogen bonding sites located at N−H···O and O−H···O within a first solvation shell of approximately 2 Å. Angular distribution functions further affirmed the relatively strong nature of the hydrogen bonds with nearly linear directionality. The increased hydroxylammonium cation (HA$^+$) mole fraction shows the influence of competitively strong hydrogen bonds on the overall hydrogen bond network. Dominant spatial motifs via three-dimensional distribution functions along with nearly nanosecond-long hydrogen bond lifetimes highlight the local bonding environment that may precede proton transfer reactions.

INTRODUCTION

Ionic liquids (ILs) are low-melting-point (≤100 °C) organic salts that, owing to their versatile thermo-physicochemical properties, have shaped the landscape of a broad number of scientific applications. Low vapor pressure and high thermal stability of ILs have led to their success as "green" solvents for biocatalysis and material processing;[1−3] non-volatility and favorable gas solubility enabled uses in lubrication,[4,5] solute removal,[6] and gas separation (e.g., CO_2 capture);[7−11] and non-flammability, wide electrochemical windows, ionic conductivity, and tunability provide promise in electrodeposition[12] and energy generation and storage applications.[13−16] Within the past two decades, ILs have also emerged as viable in-space propulsion propellants by which safer, more economical, and higher-performing thruster devices are possible. However, realizing desirable thruster performance remains a challenge and heavily depends on propellant properties. Many competing propellant breakdown mechanisms, including thermal,[17−20] catalytic,[19,21−23] or electrochemical decomposition,[24] evaporation,[25,26] or Coulombic fission,[27,28] may occur during thruster operation and produce undesirable byproducts that hinder thruster performance and lifetime during spacecraft mission operations.[29] Thus, a better understanding of fundamental IL properties is crucial for improved design and propellant selection.

To achieve mission requirements, spacecraft typically generate thrust by way of chemical or electric propulsion (EP). For several decades, chemical propulsion systems have benefited from hydrazine (N_2H_4) and its methylated derivatives (e.g., monomethylhydrazine, unsymmetrical dimethylhydrazine) as both a monopropellant and hypergolic bipropellant fuel. Hydrazine lends itself well to high-thrust propulsion devices because of its highly exothermic enthalpy of combustion, $\Delta_c H^\circ_{gas} = -622.1$ kJ mol^{-1},[30] and hypergolic, gas-phase reaction chemistry with easily stored oxidants [e.g., nitrogen dioxide, dinitrogen tetroxide, white fuming nitric acid (WFNA), etc.].[31] Moreover, heterogeneous catalysis of hydrazine with Ir and other transition metals have shown to yield spontaneous ignition [ignition delay times (IDT) of ∼10−100 ms] near room temperature with simple engineering design constraints.[32−34] However, inhaled, oral, or dermal exposure to hydrazine is extremely dangerous, thus requiring significant costs in manufacturing and handling.[35] Hence, the use of energetic ILs (EILs) with much higher heats of combustion offers a variety of green monopropellants that are less toxic, easier to store, and overall more environmentally friendly materials suited for in-space propulsion applications.[36]

In the context of chemical propulsion, EILs are typically used either as bipropellants when mixed with strong oxidants or as monopropellants, which are also referred to as "premixed oxidizer/fuel ionic propellant blends" or "self-oxidizing" EILs. Bipropellant EILs span a wide chemical composition space of either heterocyclic or ammonium-derivative cations combined with organic or inorganic, often oxygenated anions.[36−38] Various studies have sought ideal bipropellant mixtures by carefully adding N-rich functional groups for increased heats of formation without compromising liquid range or ease of handling. Some promising bipropellant candidates have mixed heteroaromatic compounds (e.g., imidazolium, triazolium, and tetrazolium),[39−43] N,N-dimethylhydrazinium,[44] or ammonium-based[45,46] cations with anions containing azido,[42,46−49] cyano,[37,50−53] borohydride,[51] and various other functional groups. Moreover, depending on miscibility, solubility, and influence on thermal and storage stability, hypergolic promoters, or transition metal or metal hydride additives can be introduced in EIL bipropellant mixtures to improve propellant hypergolicity and IDTs.[54]

Development of EIL monopropellants has posed an even greater challenge: varying different combinations of compounds and their respective concentrations influences chemical stability and compatibility, water solubility, hygroscopicity, sensitivity to impurities, and the byproducts of thermal or catalytic reactions. Previously studied EIL monopropellant formulations involve mixtures of common ionic oxidizers [e.g., hydrazinium nitrate (HN),[55−57] ammonium nitrate (AN), ammonium dinitramide (ADN),[58−60] hydroxylammonium nitrate (HAN),[61−63] etc.] with ionic fuels [e.g., ammonium azide (AA),[64] 2-hydroxyethylhydrazinium nitrate (HEHN),[65] etc.], molecular fuels (e.g., methanol, ethanol, glycerol, etc.), or sometimes polar solvents depending on solubility (e.g., water). A delicate balance of these compounds can enable the tuning of energetic and other performance-driving thermophysical properties to meet technology requirements.[66] Extensive research has led to success in formulating HAN-based and ADN-based monopropellant mixtures. For example, the most common ADN-based mixtures, FLP-106 and LMP-103S, offered enhanced energy densities, low adiabatic flame temperatures, and compatibility with stabilizing agents, like methanol, to better control burning rates.[67,68] Early HAN-based liquid gun propellants (LGPs) were found to be easily stored, characterized by hypergolic ignition behavior, and less toxic than hydrazine.[61,62,69−71] Subsequent improvements to HAN-based formulas led to AF-M315E and SHP163 that have been used successfully for in-space technology demonstrations.[72,73] Other formulations, including HNPxxx and GEM, have become increasingly relevant due to their lower adiabatic flame temperatures and success when electrically or thermally ignited (as opposed to catalytically).[56,74]

Unlike chemical propulsion, EP systems use electric energy to ionize and accelerate propellant to exhaust velocities typically on the order of 15,000 to 45,000 m/s, whereas chemical thrusters operate typically below 4000 m/s.[75] This significantly improves propellant efficiency and mass savings for space missions, while operation with fine voltage control can lead to improved thrust precision.[76] EP devices have historically used noble gases as propellant, such as xenon or krypton, because of their relatively high atomic mass, low ionization energy (and thus high ionization efficiency), and ease of handling and storage. Recently, electrospray thrusters that use high conductivity, room-temperature ILs (RTILs)

have garnered considerable attention.[77−79] Depending on RTIL properties, electrospray thrusters emit a combination of high-velocity charged ions, solvated ion clusters, and nanodroplets to generate thrust.[80]

For a spacecraft to utilize the high thrust from chemical propulsion and high efficiency from EP, separating chemical and EP systems can result in prohibitively expensive mass and cost penalties. To address this challenge, multimode propulsion (MMP) systems have been proposed as a paradigm shift in the space industry, where both propulsion technologies are integrated by using a single propellant, thereby significantly enhancing spacecraft mission flexibility and adaptability.[81] Performance of MMP systems depends critically on propellant properties: low vapor pressure, low viscosity, and high bulk density simplify thruster design; low melting points and high decomposition temperatures widens the propellant's liquid range; greater shock resistant, less corrosive, and less flammable propellants ease storage and handling.[38] For chemical propulsion, the exhaust velocity scales with the combustion temperature, $\sqrt{T_c}$, and ejected species molecular weight, $\sqrt{M}$, while the exhaust velocity for EP is proportional to the ejected species charge-to-mass ratio, $\sqrt{\frac{q}{m}}$, which is related to propellant density, ρ, surface tension, γ, electrical conductivity, κ, dielectric constant, ϵ, and flow rate, Q, by $\frac{q}{m} \propto \frac{1}{\rho}\sqrt{\frac{\gamma\kappa}{\epsilon Q}}$.[82] Finding a propellant with properties suitable for both a chemically reactive and electrically controlled environment remains a nascent and important area of research.

Attractive MMP propellants must satisfy competing trade-offs between chemical and electric propulsion for which mixture properties are not readily available or easily predicted based on individual constituent properties. For example, pure imidazolium-based ILs (e.g., [EMIM][TFSI], [EMIM][BF$_4$]) benefit electrospray operation due to higher ionic mobility, higher surface tension from better packing of small ions dominated by intermolecular, Coulombic attraction, and optimal molecular weights that minimize viscous effects of alkyl chains; however, the lack of energy-rich N−N bonds or hydroxyl groups caps heat of formation and consequently, chemical propellant thruster performance. Moreover, electrochemical and thermal degradation of many [C$_n$mim]-based ILs undergo cation−anion proton transfer that can form neutral carbene;[83] subsequent reaction pathways include vaporization or polymerization[84−87] of acidic anions that pollute thruster plumes with solid particles.[88] Alternatively, neat EILs are often protic in nature and only stable as aqueous solutions,[89] resulting in lower thermal stability and increased volatility, respectively. These properties are counterproductive for achieving high-performance EP propellants. Thus, to achieve an ideal MMP propellant, several promising formulations have been considered in the recent literature, including HAN or AN mixed with water,[90,91] nitrate salts,[92] zwitterions,[91,93] alcohols,[94] and other ILs.[95,96] Despite preliminary success of these IL-containing mixtures, even for simple, two-ion "double salt ILs" (DSILs),[97] there remain many gaps in understanding fundamental thermophysical properties and their dependence on ion structure, ion fraction, and ideal or non-ideal mixing behavior.[98,99]

Here, we investigate mixtures of two, task-specific energetic ILs, HAN and HEHN, which are of significant interest to the Air Force Research Laboratory (AFRL). In a propellant blend, HAN ($NH_3OH^+ \cdot NO_3^-$) and HEHN ($HOCH_2CH_2N_2H_4^+ \cdot$
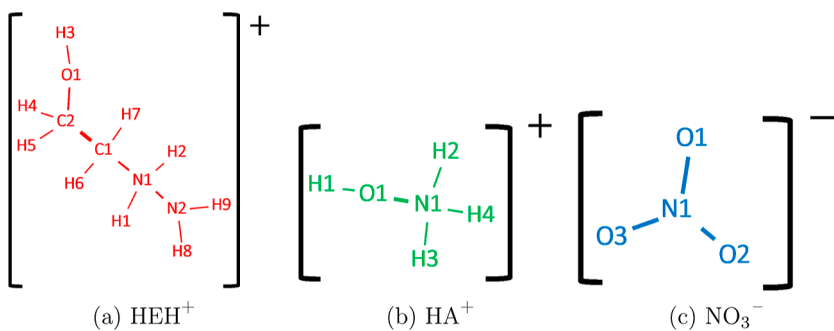
Figure 1. Chemical structure of cations and anion in pure HEHN (a,c) and HAN−HEHN mixtures (a−c).

NO_3^-) serve as complimentary ionic oxidizers and fuels, respectively, where excess oxygen from HAN can be stoichiometrically balanced by aliphatic moieties in HEHN. HAN and HEHN are composed of polar species and are expectantly miscible with each other and water; unlike purely ammonium or hydrazinium nitrates, aqueous salt mixtures of HAN are stable with relatively low concentrations of water as to avoid compromising the oxidizing effect of the nitrate anions.[61] Moreover, the energetic behavior of HAN and HEHN stems from the presence of strong hydrogen bonds between proton-donor and -acceptor sites.[100] These characteristics are akin to the broader category of protic ILs (PILs) in which numerous macroscopic properties (e.g., thermal stability, catalytic reactivity, conductivity, etc.)[101] are intrinsically linked to the liquid structure at the molecular scale. Experimentally probing the nanostructure of IL mixtures remains a challenge. While preliminary studies have observed resonant laser-based ignition[102] and reaction products from rapid-scan Fourier transform infrared (IR) spectroscopy,[103] continued theoretical and computational methods[104] are necessary to probe structural properties of HAN−HEHN mixtures.

To this end, we characterize the fundamental structural properties of HAN and HEHN through the analysis of intermolecular radial, angular, and spatial distribution functions (SDFs). We use classical, polarizable molecular dynamics (MD) simulations to study three binary HAN−HEHN mixtures at 25, 50, and 75% HAN by weight and neat HEHN for comparison. Similar simulations of HAN−H_2O systems at varied mole fractions will be reported in a companion paper. While limited experimental data are available for such mixtures, we provide comparisons for density as a function of temperature and excess molar volume curves of other ILs. Furthermore, we show that the analysis of the various calculated distribution functions elucidates the significance of hydrogen bonding. The intensity, directionality, and dominant spatial motifs of hydrogen bonds quantified and visualized in this work illustrate precursors to the rich proton transfer chemistry of energetic, protic ILs.

■ THEORY AND METHODS

The radial distribution function (RDF), typically denoted as $g(r)$, gives the average number of i neighbors in a spherical distance r around a reference particle, j. The running coordination number, $N(r)$, further quantifies the number of particles coordinating a reference atom at a specified distance r, shown in eq 1

$$N(r) = \int_0^r 4\pi\tilde{r}^2\hat{\rho}g(\tilde{r})\mathrm{d}\tilde{r} \tag{1}$$

where $\hat{\rho}$ = N/V is the average number density of the observed atom (in $Å^{-3}$). The SDF calculates the pair-wise correlations in three-dimensional space, thus providing a global perspective of the coordination of two atoms in a given system. Previous studies have used RDFs and SDFs to give extensive insights into the local behavior of ILs.[105] For instance, RDF data provide signatures of strong, cation−anion Coulomb interactions that enhance short-range structuring (2−5 Å) and influence mixing.[106] Oscillatory behavior in ILs is also observed at longer ranges (6−8 Å) which provide important charge correlation attributes.[107]

To accurately model the relevant chemical interactions for ILs, generally, various interatomic potentials have been used, ranging from united-atom,[108] all-atom nonpolarizable,[109,110] to polarizable[111−113] force fields. In the excellent review by Bedrov et al.,[105] it was found that to predict numerous IL electrostatic and transport properties accurately, polarizability, or the response of electronic density to a local electric field, was essential. Several polarizable models have been proposed, from mean-field treatments, and classical Drude oscillators, to induced point dipole methods. The simulations herein use the induced point dipole method implemented in APPLE&P, a software previously developed for a wide range of ILs validated against experimental and quantum mechanical data.[113−115]

All condensed-phased MD simulations were performed using the original APPLE&P force field[113] with reparameterized repulsion−dispersion terms using a HEHN/HAN/H_2O dataset of quantum chemical (QC) calculations.[20] As previously mentioned, a companion paper explores HAN−H_2O systems at varied mole fractions, whereas in this work, the same force field was used to explore HAN−HEHN systems. The functional form used to define the interatomic potential energy is provided in eq S1.

Each liquid phase simulation consisted of a finite number of HEHN or HAN cations and anions, shown in Figure 1. The domain was first initialized by using a custom system generation code in Python, where a periodic three-dimensional box was created with about 1.5 times the target dimensions. Neat HEHN was composed of 400 HEH^+ and 400 NO_3^- ions; the HAN−HEHN mixture consisting of 50% of each species by weight fraction was composed of 212 HA^+, 147 HEH^+, and 359 NO_3^- (i.e., 0.59 mole fraction of HAN). Briefly, 0.1 ns isokinetic cell compression simulations at high temperatures (~450 K) were conducted until a target box volume was achieved based on an approximate density. Isokinetic velocity scaling was used to achieve a target temperature ranging from 250 to 450 K. Subsequent equilibration runs were conducted

in the isothermal−isobaric (NPT) ensemble until converged densities were obtained. Equilibrium cell sizes for each system are shown in Figure 2. Longer, ∼10 ns production runs in the
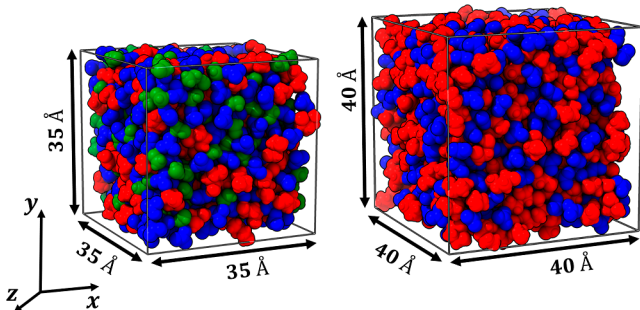
Figure 2. Bulk phase system configuration of 50−50% HAN−HEHN mixture (left) and pure HEHN (right).

NPT ensemble were used for analyzing structural properties. NVT calculations sampled from the NPT results were used to later calculate dynamic properties (i.e., mean squared displacement, self-diffusion coefficients, etc.) and will be the emphasis of future work. The NPT ensemble is initially chosen as this most closely relates statistical mechanics to thermodynamic conditions in the experiment, resulting in an equilibrium system (constant potential energy, converged density, etc.) that can be sampled in the canonical ensemble.[116]

In each simulation, temperatures and pressures were controlled by a Nosé-Hoover thermostat and barostat. All covalent bonds (lengths) were constrained using the SHAKE algorithm.[117] Long-range electrostatic calculations (i.e., interactions between any two atomic partial charges or between partial charges and induced dipoles) were determined by the Ewald summation method using 8^3 k-vectors and α of 0.24 Å. Induced dipoles were computed using the predictor−corrector method. The "polarization catastrophe"[114] was avoided by Thole screening ($\alpha_T = 0.2$) to smear the charge distribution and effectively dampen the induced dipole−induced dipole interactions. The MD integrator was performed over multiple time step values, where 0.25 fs was used for bonded interactions, 1.5 fs for nonbonded interactions within a 7.0 Å truncation, and 3.0 fs for nonbonded interactions outside of the 7.0 Å truncation but within the dispersion cutoff radius of 13.0 Å and the reciprocal terms of the Ewald summation. The trajectory information was recorded every 1500 fs.

■ RESULTS AND DISCUSSION

Density. The liquid densities as a function of temperature and mole fraction for both the neat HEHN and HAN−HEHN mixtures are provided in Figures 3 and 4. The uncertainties (not plotted) are provided by the standard deviations obtained from the normally distributed density data collected throughout the equilibration simulations, as shown in Figure S1 and tabulated in Table S1 in the Supporting Information section. All simulation uncertainties (2σ) were less than 1% of the mean value. The simulated neat HEHN density is 1.391 g cm^{-3} at room temperature (298 K) and 2.0% within the reference value, 1.420 g cm^{-3}.[118] The force field employed in this work was trained using the procedure described by Borodin.[119] Fitting the repulsion−dispersion parameters required a tradeoff between density and transport property timescales. Thus, the simulated density value below 2.0% was
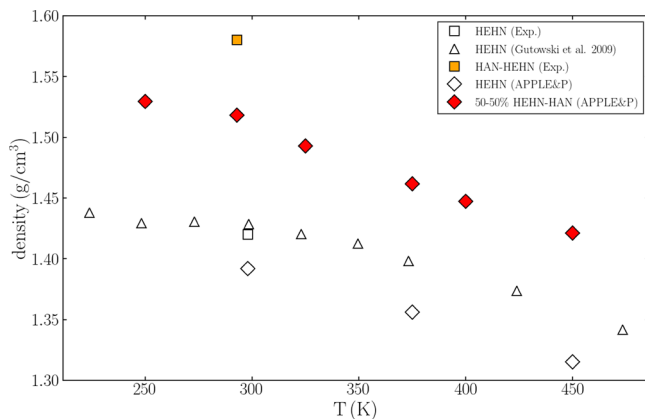
Figure 3. Comparison between experimental and predicted condensed-phase density values as functions of temperature. Pure HEHN values include experimental[118] (□), polarizable (◇), and nonpolarizable[120] (△) simulations; 50−50% HAN−HEHN values include experimental (orange ■) and polarizable (red ◆) simulations.
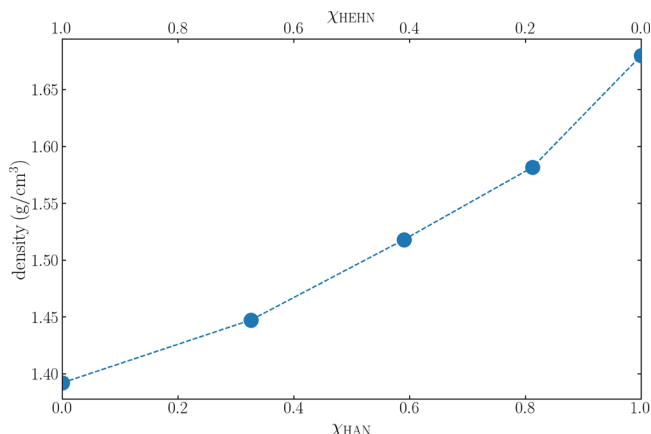
Figure 4. Simulation results for density as a function of HEHN and HAN mole fraction at room temperature (the 50−50% HAN−HEHN was conducted at 293 K to match the experimental measurement, while every other "room temperature" calculation was at 298 K). Density of pure HAN ($\chi_{HEHN} = 0.0$) is based on an experimental reference value of 1.68 g cm^{-3} for anhydrous HAN,[121] for which no temperature value was reported but is expected to be near the HAN melting point, 44−48 °C.[122]

expected, especially when the purity of "neat" HEHN and the density measurement's overall systematic errors were not reported by the authors.[118] At and above room temperature (298 K), the near-linear trend of decreasing density as a function of temperature is consistent with nonpolarizable force fields reported by Gutowski et al.[120]

The influence of HAN in the HAN−HEHN mixture is evident by the 7−9% increase in density compared to the neat HEHN system. As will be shown in later results, the increased density is indicative of the strong hydrogen bonding between the nitrate oxygen and the hydrogens of HAN hydroxyl and amine groups. It is noted that no thermophysical data exists for a purely HAN−HEHN mixture, so a density measurement for a propellant (50% HEHN, 46.5% HAN, and 3.5% minor organic/inorganics by weight) at 293 K was reported for comparison. The simulated HAN−HEHN mixture density is 3.8% below the experimental HAN−HEHN propellant, which is in acceptable agreement without the need for further force field parameterization.

The mole fraction-dependent density plot in Figure 4 is consistent with this trend as shown by the nearly inverse relationship between density and χ_{HEHN}. The increase in density at increased χ_{HAN} can be attributed to the significant increase in overall inter-ion Coulombic attractive forces driven by the more compact and polar HA$^+$ cation relative to the large, bulky HEH$^+$ cation. For reference, preliminary HEHN−H$_2$O experimental and predicted values are reported in Figure S2 to show consistency in density value order-of-magnitudes. To further explain the non-linear and non-ideal mixing behavior of HAN and HEHN observed in Figure 4, the excess molar volume, V_m^E, of the mixture was investigated. As shown in eq 2, V_m^E quantifies the difference between the actual mixture molar volume and the individual constituent molar volumes

$$V_m^E = \frac{\chi_{HAN}M_{HAN} + \chi_{HEHN}M_{HEHN}}{\rho_{HAN-HEHN}} - \frac{\chi_{HAN}M_{HAN}}{\rho_{HAN}}$$
$$- \frac{\chi_{HEHN}M_{HEHN}}{\rho_{HEHN}} \quad (2)$$

where χ, M, and ρ are the mole fractions, molar masses, and densities of the constituents in the subscripts, respectively.[97] While no previous experimental studies have investigated V_m^E for HAN−HEHN, select DSIL systems are included in Figures 5 and S3 for comparison. The Redlich−Kister polynomial
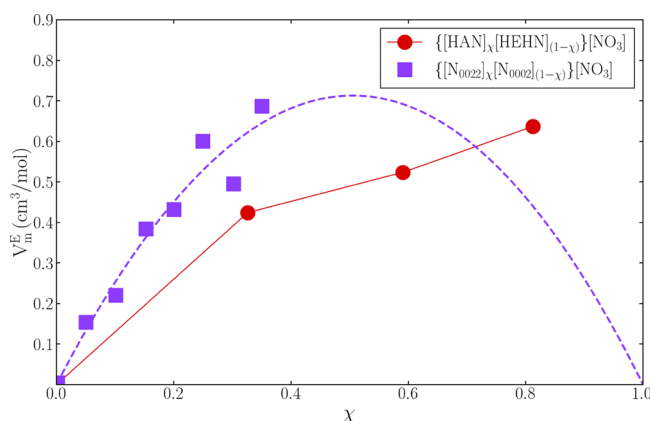
Figure 5. Calculated excess molar volume of the (red ●) HAN−HEHN mixture. Experimental comparison includes a three-ion DSIL mixture of (purple ■) nitrate anions (NO$_3$) with ethylammonium (N$_{0002}$) and diethylammonium (N$_{0022}$) cations and associated Redlich−Kister curve fit (dashed lines) as a function of N$_{0022}$ mole fraction.

functional form,[123] shown in eq 3, was used to find the order, n, and coefficients, C_n, that characterize the overall relationship between V_m^E and χ (only for systems with sufficient number of data points to generate reliable fits)

$$V_m^E = \chi(1-\chi)\sum_n C_n(1-2\chi)^{n-1} \quad (3)$$

The positive V_m^E values predominantly below 1.0 cm^3 mol^{-1} and qualitatively similar profile as the Redlich−Kister fit with downward concavity are in good agreement with numerous IL mixtures that resemble three-ion DSILs, where both components share either a cation or anion.[124−128] Figure 5 compares HAN−HEHN with one other PIL, $\{[N_{0002}]_\chi[N_{0022}]_{(1-\chi)}\}[NO_3]$, and Figure S3 compares two additional aprotic ILs, $[EMIM]\{[BF_4]_\chi[TFSI]_{(1-\chi)}\}$ and

$[EMIM]\{[EtSO_4]_\chi[TFSI]_{(1-\chi)}\}$. While a complete, quantitative understanding of excess molar volume trends across various DSIL compositions is still poorly understood, Figure 5 further substantiates the hypothesis that molecular weight and volume of the uncommon ion contribute to non-ideal mixing behavior.[97] For example, Canongia Lopes et al.[129] observe that in mixtures like ethylammonium (N$_{0002}$) and diethylammonium (N$_{0022}$) nitrate, increasing the number of ethyl groups (i.e., N$_{0222}$, N$_{2222}$, etc.) results in larger maximum V_m^E magnitudes. Similarly, the disparate cation size and shape of the HA$^+$ and HEH$^+$ cations can, as Castejón and Lashock describe, disrupt the configurational entropy of mixing, thereby resulting in positive excess molar volumes.[130] Interestingly, the non-ideal mixing behavior persists at larger HAN mole fractions past the equimolar point, resulting in apparent asymmetry. As was mentioned previously, HAN cation−anion pairs experience an extremely strong intermolecular attraction that favors nucleation and highly organized structuring at room temperatures. Figure 5 indicates that steric hindrance effects of HEHN at even low mole fractions may impede the long-range ordering of a HAN Coulomb lattice.[97,101]

Structural Properties. *Radial Distribution Functions. Center of Mass RDFs.* As stated earlier, the local structure provides critical insights into the macroscopic behavior of an IL mixture. RDFs describe the local density distribution of atoms around a reference point of interest. Concretely, an RDF, $g(r)$, quantifies the probability density of finding a pair of atoms (or a pair of chemical species) a distance r apart. In general, the cation−anion Coulomb interactions dictate local structure that ultimately influences the length-scale of long-range repulsive interactions between the cation−cation and anion−anion pairs. The following RDFs were calculated using an open-source software, TRAVIS.[131] To begin, the ion center of mass (COM) RDFs for the HEHN and HAN−HEHN (50−50% weight) systems are shown in Figure 6 and the peaks and intensities are summarized in Table 1.

The relative arrangement of COM RDF peaks can be described in relation to the primitive model of molten salts originally presented by Hansen and McDonald.[132] In two-component, anisotropic ionic solutions composed of hard-sphere-like ions (e.g., NaCl), three well-defined peaks are present at short-range, while long-range correlations persist for a few characteristic ion length scales; the two like-species peak in nearly out-of-phase behavior with the cation−anion pairs, where maxima in the former align with minima in the latter. In the case of Figure 6a, the most notable feature is the proximity ($r = 4.75$ Å) and intensity ($g(r) = 2.62$) of the cation−anion [HEH]$^+$−[NO$_3$]$^-$ coordination relative to all other RDFs. The HA$^+$, a more compact polar cation than HEH$^+$, results in an even closer ($r = 3.95$ Å) and larger peak ($g(r) = 4.69$), as shown in Figure 6b. The lack of a great difference between the two [HEH$^+$]−[NO$_3^-$] curves (shown in blue) between pure HEHN and HAN−HEHN shows that the coordination distances are largely unaffected by increased HA$^+$.

Unlike Na$^+$, however, the HEH$^+$ cation can exhibit significant charge delocalization that induces short-range (∼7 Å) cation−cation and anion−anion ordering. The like-species in bulk-phase HEHN deviate from behavior observed in the primitive model largely due to the highly non-spherical conformations of the HEH$^+$ cation; the out-of-phase behavior will be more apparent in atomistic RDFs shown in subsequent sections to highlight the effects of diffused charge across the

(a)

(b)
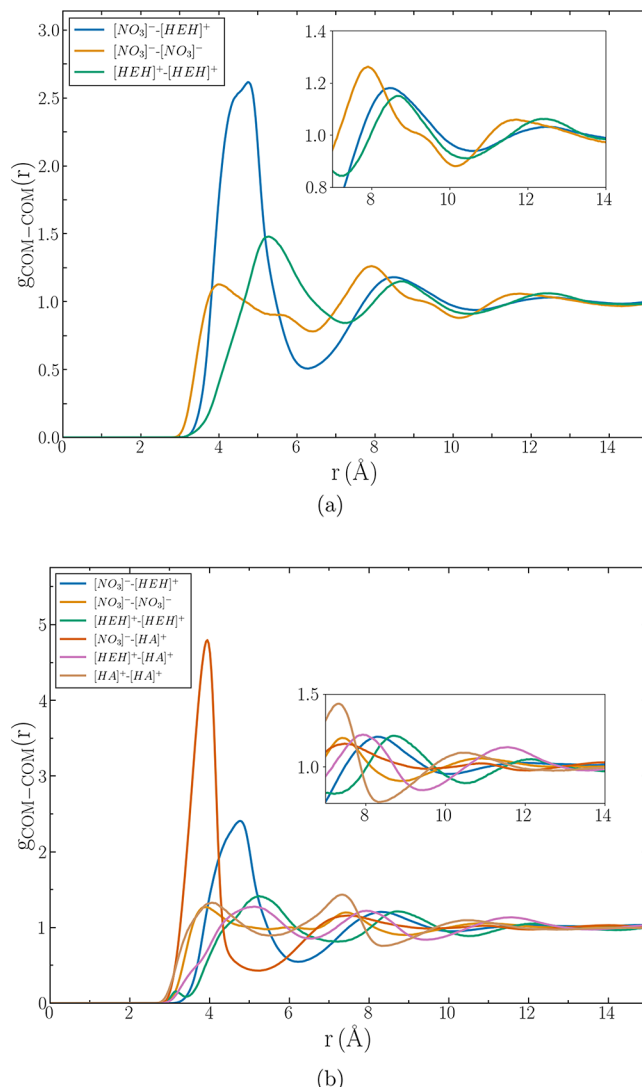
Figure 6. Center of mass RDFs for intermolecular species coordination in (a) pure HEHN at 298 K and (b) 50−50% HAN−HEHN at 293 K.

Table 1. Pure HEHN (Top) and 50−50% HAN−HEHN (Bottom) Peak Distances, Å, and Intensities from Center of Mass Radial Distribution Functions

	1st peak	2nd peak
$HEH^+-NO_3^-$	4.75 Å (2.62)	8.49 Å (1.18)
	4.78 Å (2.38)	8.34 Å (1.18)
$HA^+-NO_3^-$		
	3.95 Å (4.69)	7.45 Å (1.15)
HA^+-HA^+		
	4.05 Å (1.32)	7.35 Å (1.40)
HEH^+-HEH^+	5.25 Å (1.48)	8.76 Å (1.15)
	5.20 Å (1.37)	8.76 Å (1.17)
$NO_3^--NO_3^-$	3.99 Å (1.13)	7.92 Å (1.27)
	3.92 Å (1.24)	7.44 Å (1.18)

HEH^+ species among the hydroxyl and amine functional groups. For instance, the HEH^+ has up to three possible coordination sites near the positively-charged nitrogen (N_1), terminal nitrogen (N_2), and hydroxyl group (O_1-H_3). As will be visualized in later sections, multiple anions coordinating with the same HEH^+ cation results in the weak $[NO_3]^--$

$[NO_3]^-$ peak at ~4 Å. Similarly, the secondary $[HEH]^+-[HEH]^+$ peak is due to a cation−anion-cation arrangement commonly found in other room-temperature ILs.[114]

While the short-range structure is evidently species-dependent, theoretical findings support long-range behavior to be similar across various ILs and molten salts. The zoomed-in view of the long-range correlations in both HEHN and HAN−HEHN systems in Figure 6 shows ordering up to ~15 Å; however, the lack of out-of-phase oscillations between like and unlike ions is likely due to the COM poorly representing the delocalized charge. It is well known that at long-range, charge ordering in ILs is a result of either hard-packing or electrostatic screening of ions, a behavior that most notably obeys the charge-neutrality sum rule[133]

$$\int_0^r 4\pi r'^2 \left[\sum_\mu q_\mu \rho_\mu g_{\mu\nu}(r') \right] dr' = -q_{sum}^\nu(r) \quad (4)$$

where μ and ν is the ion label (i.e., either the reference cation or anion), ρ_μ is the ion number density, $g_{\mu\nu}(r')$ is the ion−ion COM RDF, and r is the radial distance away from a centered ion which includes the net charge, q_{sum}. In the limit $r \to \infty$, $|-q_{sum}^\nu| = 1$ by charge neutrality. Figure 7 shows the charge
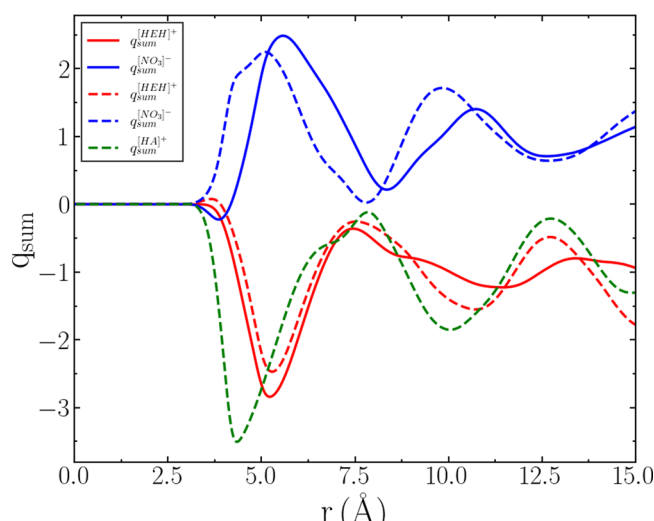
Figure 7. Charge oscillations (eq 4) in a neat HEHN (solid lines) and 50−50% HAN−HEHN (dashed lines) system.

oscillations up to 15 Å for the pure HEHN and HAN−HEHN systems. The qualitative, anti-correlated behavior illustrates the tendency for anions to surround the cations in, spherical, ion shells. Within bulk HEHN, the enclosed charge surrounding the HEH^+ cation, q_{sum}^{HEH+} oscillates between $-2.85 < q_{sum}^{HEH+} < 0.0$. Upon addition of HA^+, a slight decrease in q_{sum}^{HEH+} range to $-2.50 < q_{sum}^{HEH+} < 0.1$ and notable q_{sum}^{HA+} range of $-3.50 < q_{sum}^{HA+} < 0.0$ was observed. This shift in q_{sum}^{HEH+} is indicative of the HA^+ cation out-competing the HEH^+ cation for anion packing. The long-range oscillations of q_{sum}^{HA+} are most reminiscent of patterns observed in molten salts.[107]

Cation−Anion Atomistic RDFs. As was previously mentioned, the COM of the HEH^+ does not overlap with its charge center due to charge delocalization. The atomistic RDFs

provide a clearer illustration of the delocalized charge across the HEH$^+$ that influences its unique short-range ordering. The representative atomistic RDFs for the HEHN and 50−50% HAN−HEHN system are shown in Figure 8, where each curve
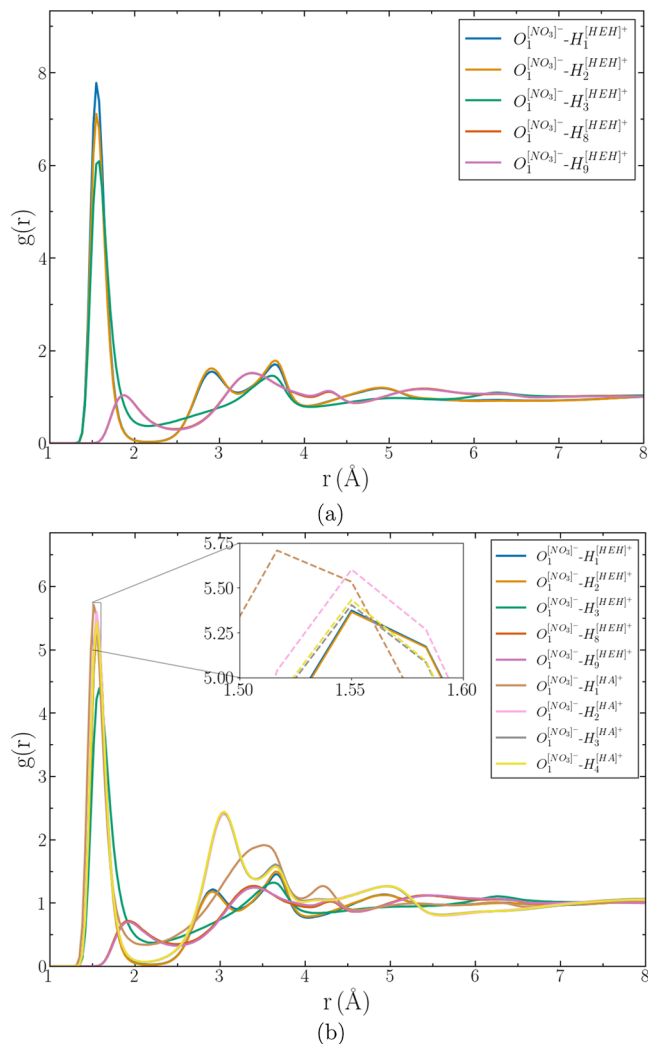
Figure 8. Atomistic RDFs for $O_1^{NO_3^-}$−H correlations for hydrogen atoms in hydroxyl and amine moieties on (a) pure HEHN and (b) 50−50% HAN−HEHN cations. The solid and dashed lines represent atom pairs of NO_3^- and either the HEH$^+$ or HA$^+$ cation, respectively.

elucidates the preferred positioning of the (negative) oxygen of the nitrate relative to a specific cation hydrogen. Peak distances and heights are tabulated in Table 2.

The most notable feature in both Figure 8a,b are the relatively short coordination peak distances found within a ∼2 Å first solvation shell. In this work, the first solvation shell refers to the coordination environment around a reference atom (or molecule) up to the first minimum in an RDF. Hydrogen-mediated, noncovalent interactions of this strength are widely classified as hydrogen bonds (H-bonds) within protic ILs, where an H-bond X−H⋯Y contains a proton donor, X−H, and acceptor, Y.[134] In the case of neat HEHN, the acidic NH moiety on the substituted-amine and the oxygen atom on the hydroxyl group form strong, doubly ionic H-bonds[97] with the nitrate oxygen atom, N_1−$H_{1,2}$⋯O and O_1−H_3⋯O, respectively. Relative to the range of H-bond distances that naturally form in water (∼1.45 Å[135]) to common aprotic

Table 2. Pure HEHN (Top) and 50−50% HAN−HEHN (Bottom) Peak Distances, Å, and Intensities from Atomistic Radial Distribution Functions with $O_1^{NO_3^-}$ Set as Reference

	1st peak	2nd peak	3rd peak
$H_1^{HEH^+}$	1.55 Å (7.79)	2.92 Å (1.55)	3.65 Å (1.68)
	1.55 Å (5.10)	2.92 Å (1.21)	3.65 Å (1.43)
$H_2^{HEH^+}$	1.55 Å (7.18)	2.92 Å (1.62)	3.65 Å (1.76)
	1.55 Å (5.51)	2.92 Å (1.12)	3.65 Å (1.45)
$H_3^{HEH^+}$	1.58 Å (6.04)	3.62 Å (1.46)	
	1.58 Å (4.16)	3.62 Å (1.30)	
$H_8^{HEH^+}$	1.88 Å (1.02)	3.38 Å (1.51)	
	1.92 Å (0.73)	3.42 Å (1.26)	
$H_9^{HEH^+}$	1.88 Å (1.00)	3.38 Å (1.53)	
	1.95 Å (0.69)	3.35 Å (1.22)	
$H_1^{HA^+}$			
	1.52 Å (5.59)	3.52 Å (1.86)	
$H_2^{HA^+}$			
	1.55 Å (5.37)	3.05 Å (2.35)	
$H_3^{HA^+}$			
	1.55 Å (5.45)	3.05 Å (2.36)	
$H_4^{HA^+}$			
	1.55 Å (5.25)	3.05 Å (2.43)	

ILs (≳2.2 Å), the N_1−H⋯O and O_1−H⋯O RDFs in Figure 8a indicate very strong H-bonding (1.55−1.58 Å) in neat HEHN. While the subtle difference between N_1−H_1⋯O and N_1−H_2⋯O RDFs is likely due to finite sampling effects, the more pronounced decrease of the O_1−H_3⋯O RDF height is due to a majority of the cationic charge located in the substituted-amine group. This trend is nearly reversed in the case of the HA$^+$ cation (dashed lines, Figure 8b). While the HAN O_1−H_1⋯O H-bond (dashed brown curve) has an arguably insignificant increase in intensity relative to the amine-group H-bonds (pink, yellow, and gray dashed lines), our companion paper elaborates on such a trend for various HAN−H_2O systems. The N_2−$H_{8,9}$⋯O RDFs are significantly less intense and their peak distances of ∼1.9 Å are a secondary peak to the N_1−H_1⋯O H-bond. The locations of these H-bonding donor/acceptor sites are consistent with collision-induced dissociation (CID) measurements[96] and recent IR spectra and ab initio molecular dynamics (AIMD) simulations[136] of small, solvated cation clusters, $(HEH^+)_n(NO_3^-)_{n-1}$.

Figure 8b shows atomistic RDFs for the 50−50% wt. HAN−HEHN system, where four additional coordination sites are introduced within a similar first solvation shell as observed in the neat HEHN. While the coordination distances remain effectively unchanged, Figure 8b and Table 2 confirm the clear competition between H-bonding sites based on the overall reduced intensities of the peaks. The strongest correlation is between nitrate O_1 and H_1 of HA$^+$, and the H_1 of HEH$^+$ competes with the H_{2-4} of HA$^+$ and H_2 of HEH$^+$ for the nitrate. The HA$^+$ presents a more accessible cation for acceptor sites on the nitrate oxygen, thereby out-competing H-bond donor/acceptor sites found predominantly in neat HEHN. Such H-bonding behavior within IL mixtures has explained the non-ideal mixing similarly observed in Figure 5 from earlier sections.[137−139]

Mole Fraction Dependence and Cation−Cation Interactions. To further investigate the H-bond intensity, the unnormalized atomistic RDFs in Figure 9 were analyzed, which show that while the qualitative behavior of the distributions remains the same, the peak heights are heavily dependent on
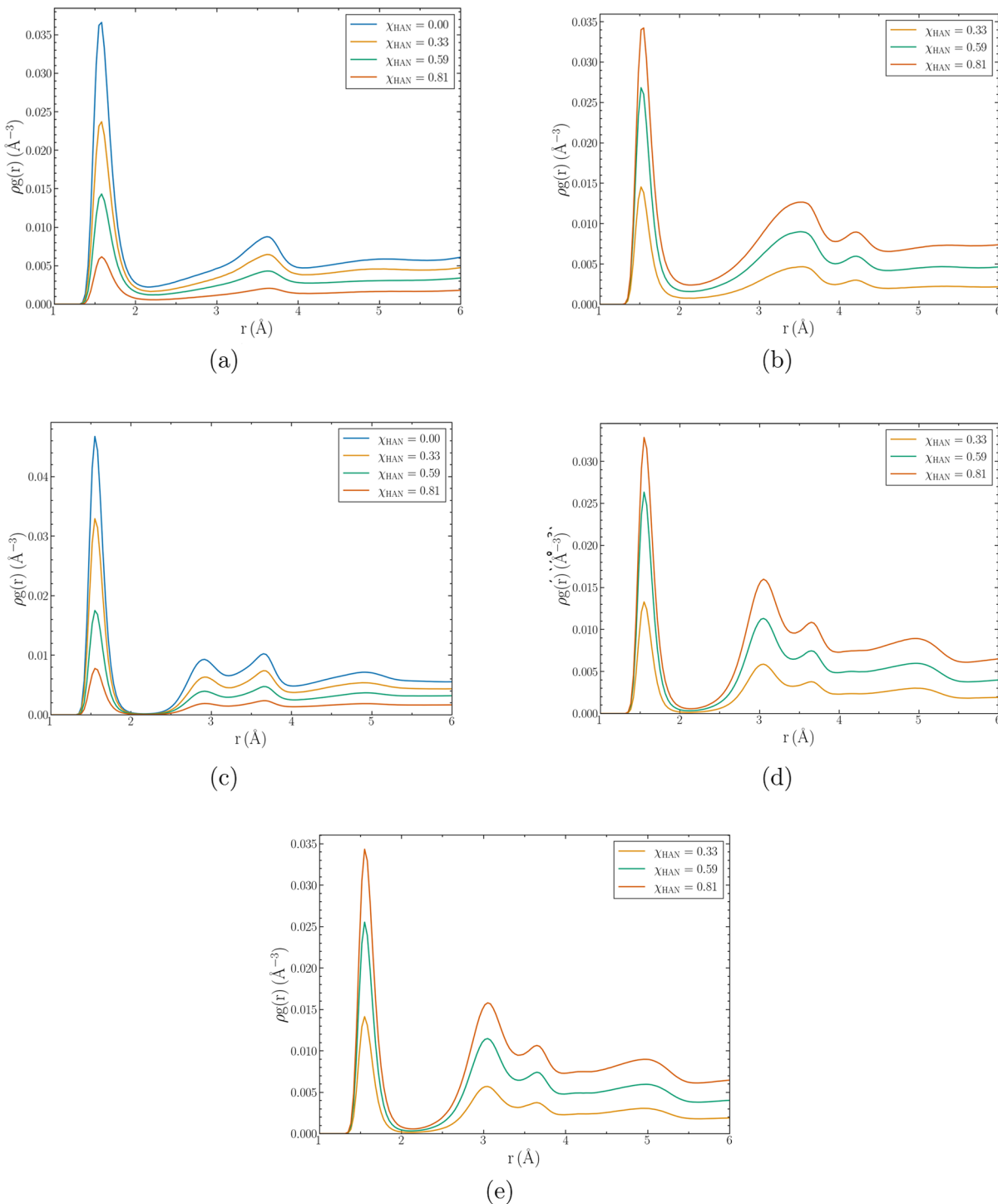
Figure 9. Probability distributions of hydrogen bond donor/acceptor sites as a function of HAN mole fraction. (a) H_3 (HEH^+)$-O_1$ (NO_3^-), (b) H_1 (HA^+)$-O_1$ (NO_3^-), (c) H_1 (HEH^+)$-O_1$ (NO_3^-), (d) H_2 (HA^+)$-O_1$ (NO_3^-), and (e) H_4 (HA^+)$-O_1$ (NO_3^-).

HAN mole fraction. Specifically, all H-bonds between HEHN ions (Figure 9a,c) exhibit monotonically decreasing ion coordination strength as a function of χ_{HAN}. The opposite is true for H-bonds between HAN ions (Figure 9b,d,e). The exact peak heights and respective trends are provided in Figure S4. Interestingly, the diminishing $HEH^+\cdots NO_3^-$ H-bonds at increased HAN mole fractions give rise to cation−cation interactions previously observed experimentally in various, similar ILs.[96,136] Although Zeng et al.[136] discovered this motif in small charged clusters of neat HEHN, no significant

structuring between two neighboring HEH^+ was observed in the bulk, net-neutral simulations at $\chi_{HAN} = 0$. At higher χ_{HAN}, however, Figure 10 shows the increase in coordination between neighboring HEH^+ hydroxyl and HA^+ amine groups, i.e., the $(HA^+)N_1-H_{2-4}\cdots(HEH^+)O_1$ H-bonds. The consequence of H-bond competition for any labile HA^+ donors unable to coordinate with nitrate oxygen leaves the nearby lone electron pairs on $(HEH^+)O_1$ as a partially negative acceptor site.
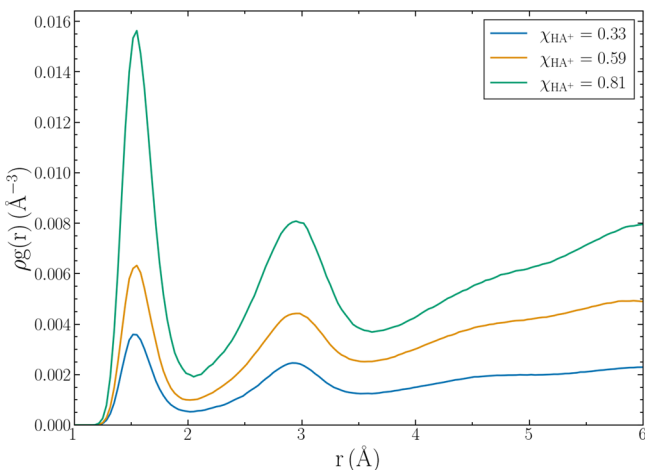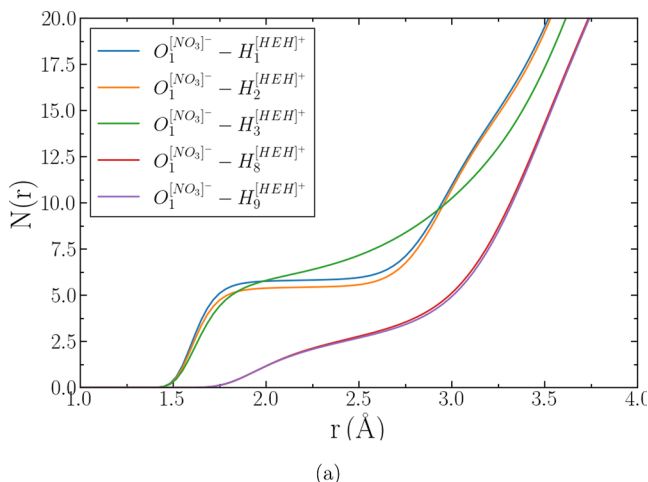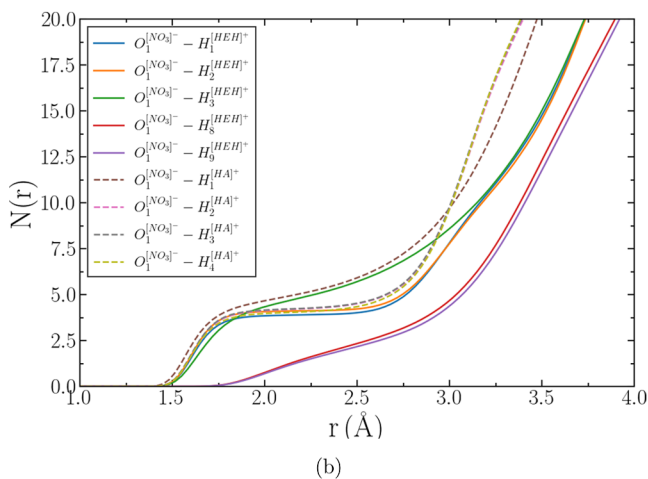
Figure 10. Probability distribution functions for the inter-cation H-bonding site, $(HA^+)N_1-H_{2-4}\cdots(HEH^+)O_1$.

Cation−anion interactions in Figure 8 can enable calculating the coordination number within the first coordination shell of the HEH$^+$ and HA$^+$ cations. The running coordination plots in Figure 11 and the values summarized in Table 3 show that in pure HEHN, it is the H$_1$, H$_2$, and H$_3$ hydrogens in the HEH$^+$

Table 3. Pure HEHN (Top) and 50−50% HAN−HEHN (Bottom) First Solvation Shell Distances, r_{min} in Å, and Corresponding Coordination Numbers in Terms of the Number of Atoms Surrounding $O_1^{NO_{3^-}}$ Set as Reference

	r_{min} (Å)	$N(r_{min})$
$H_1^{HEH^+}$	2.15	5.81
	2.18	3.89
$H_2^{HEH^+}$	2.15	5.43
	2.21	4.12
$H_3^{HEH^+}$	2.15	6.23
	2.18	4.87
$H_8^{HEH^+}$	2.48	2.81
	2.52	2.48
$H_9^{HEH^+}$	2.48	2.73
	2.48	2.21
$H_1^{HA^+}$		
	2.08	4.89
$H_2^{HA^+}$		
	2.08	4.18
$H_3^{HA^+}$		
	2.12	4.22
$H_4^{HA^+}$		
	2.08	4.02

as well H$_{1-4}$ hydrogens of HA$^+$ in the mixture that influence the structure in the first solvation shell of ∼2.15 Å.

Angular Distribution Functions. Moreover, angular distribution functions (ADFs) have also been calculated to examine the directionality of the H-bonds identified from the atomistic RDFs. The total number of each angle after an applied cone correction was computed and then normalized to obtain a probability distribution, $p(\theta)$. Figure 12 shows the $p(\theta)$ for all H-bonds in the 50−50% HAN−HEHN mixture within their respective first solvation shells. Overall, all hydrogen bonds show maxima at 180°, indicative of linear directionality. Regardless of the cation species (i.e., for both HA$^+$ and HEH$^+$), H-bonds with positive nitrogen centers as their donors, N$_1$−H⋯O$_1$, show the sharpest distributions,

(a)

(b)

Figure 11. Running coordination numbers, $N(r)$, corresponding to atomistic RDFs for (a) HEHN (ρ = 0.107 Å^{-3}) and (b) 50−50% HAN−HEHN (ρ = 0.109 Å^{-3}).
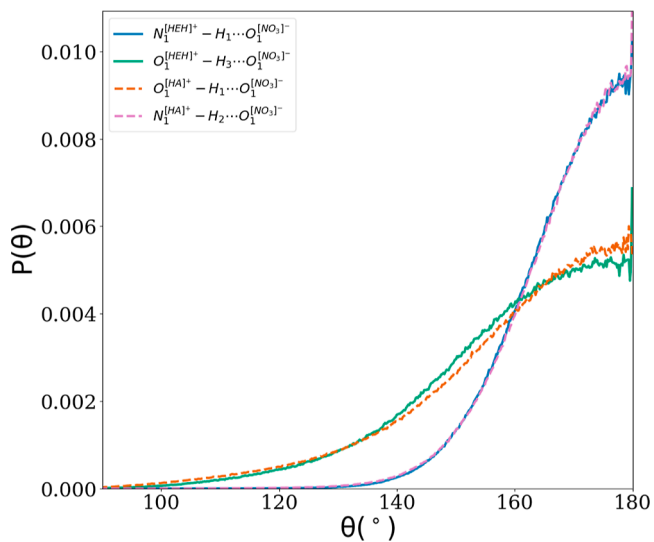
Figure 12. ADFs for strong H-bonds for the 50−50% HAN−HEHN system. Based on Figure 8, the associated initial peak heights for each curve are at 1.55 Å (solid blue), 1.55 Å (dashed pink), 1.58 Å (solid green), and 1.52 Å (dashed orange).

while the $O_1-H\cdots O_1$ are the broadest. Figures 8b and 12 together support the notion that strong, linear H-bonds play a significant role in the overall structural properties of mixed HEHN and HAN.

Spatial Distribution Functions. Figures 13 and 14 depict isosurfaces of the three-dimensional, SDFs for the neat HEHN
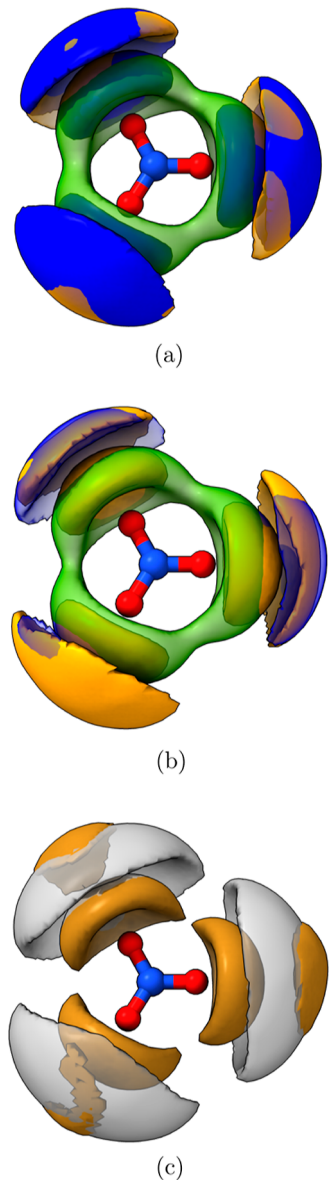
Figure 13. SDFs in HEHN (13a) and 50−50% HAN−HEHN (b,c) mixtures around the NO_3^- anion. Isosurface colors coincide with target atoms shown in Figure 8 legend. (a) NO_3^- SDF in pure HEHN with H_1 (blue), H_2 (orange), and H_3 (green) target atoms from HEH$^+$. (b) NO_3^- SDF in 50−50% HAN−HEHN with H_1 (blue), H_2 (orange), and H_3 (green) target atoms from HEH$^+$. (c) NO_3^- SDF in 50−50% HAN−HEHN with H_1 (brown) and H_3 (gray) target atoms from HA$^+$.

and 50−50% HAN−HEHN mixture. SDFs provide detailed qualitative information about ion coordination. Local regions surrounding the HA$^+$ and HEH$^+$ cations of a selected oxygen atom on the nitrate anion can be found. The isosurface colors of Figure 13 align with the atomistic RDF legend in Figure 8.

In Figure 13, three, well-defined lobes of preferable cationic hydrogen positions form around the nitrate oxygen. Both the
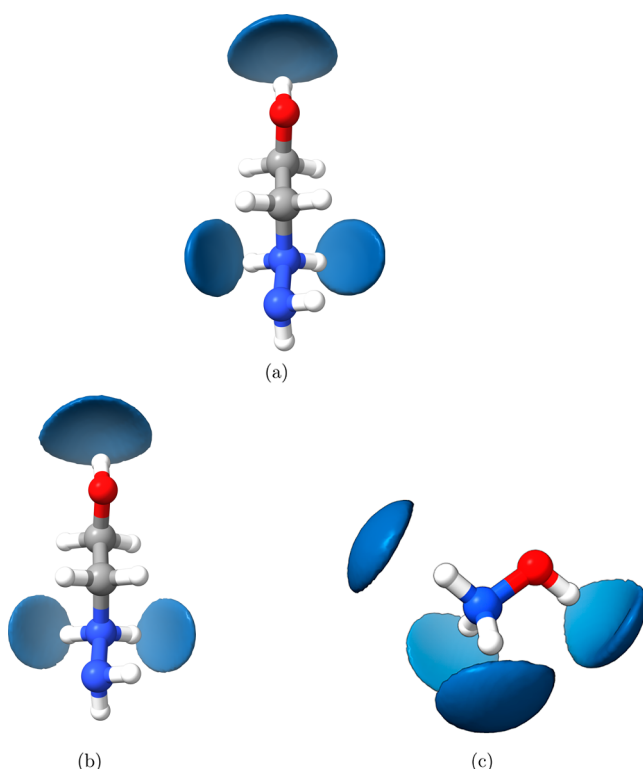
Figure 14. SDFs in HEHN (a) and 50−50% HAN−HEHN (b,c) mixtures around the HEH$^+$ and HA$^+$ cations. Ocean blue isosurfaces indicate preferential positioning of O_1 of the nitrate oxygen.

first and second solvation shells are visible. For the first solvation shell, i.e., the innermost lobes near the nitrate oxygen, all three HEH$^+$ hydrogens, H_{1-3}, are represented; any of the respective colors (blue, orange, and green) not visible in Figures 13a,b is due to overlapping isosurfaces. The linear nature of the HEH$^+$ $N_1-H_{1,2}\cdots O_1$ H-bonds driven by strong Coulombic attraction is evident in Figure 13a. The smooth and connected $O_1-H_3\cdots O_1$ isosurface in green resembles the smearing of the ADF observed in Figure 12. Thus, H-bonds between nitrate oxygen and HEH$^+$ amine groups are stronger than with hydroxyl groups, resulting in a broader, local rearrangement of $O_1-H_3\cdots O_1$ H-bonding.

The addition of 50% HAN by weight results in largely the same spatial ordering for the $N_1-H_{1,2}\cdots O_1$ and $O_1-H_3\cdots O_1$ interactions between HEH$^+$ and NO_3^-, as shown by Figure 13b. The power of visualizing SDFs lies in Figure 13c, where both the HA$^+$ H_1 and H_3 (which appears identical to any other ammonium hydrogen, H_2 or H_4) show three distinct lobes similar to the $N_1-H_{1,2}\cdots O_1$ lobes in Figure 13a,b. Consequently, the SDFs show that within the bulk liquid, a nitrate anion is surrounded by up to seven (H_{1-4} of HA$^+$ and H_{1-3} of HEH$^+$) possible H-bonds competing for coordination within the first solvation shell (of ∼2 Å). While the lobes within the first solvation shell appear to overlap, their subtle asymmetry can be explained by their inherent coupling, or anticooperativity, with one another in the bulk.[134] In this case, when the nitrate oxygen acts as a double acceptor, one H-bond is locally stronger than the second donor.

Figure 14 visualizes the alternate SDF from the reference frame of the cation as it coordinates with the nitrate oxygen. In both HEHN and 50−50% HAN−HEHN from Figure 14a,b, respectively, the spatial orientation of the nitrate oxygen

(ocean blue isosurface) shows a similar behavior: two primary coordination sites are present near the substituted amine and hydroxyl group. The SDF isosurfaces closest to the amine groups generate lobes with a convex bulge around the N_1 H-bond donor as expected from the atomistic RDF results. The lobes around the hydroxyl group show in 3D the relatively broader angular distribution—because the nitrate oxygens have two lone pair electrons, bifurcated H-bonding is possible at this site. Overall, the isosurfaces in Figure 14a,b elucidate the highly local and anisotropic nature of the HEH^+ coordination environment, for which COM−COM RDFs or common coordination numbers derived from spherical integration are not ideally suited. A representative geometry from Figure 15 shows this manifesting in a sampled
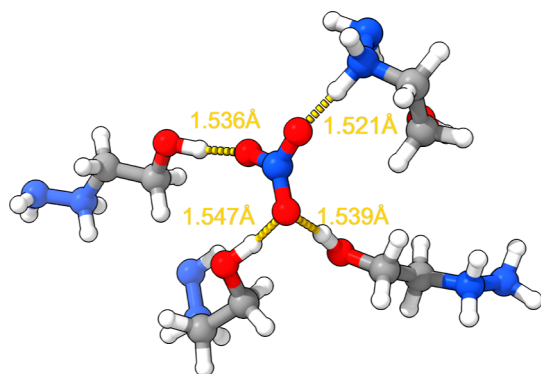
Figure 15. Representative geometry of bulk-phase, neat HEHN with coordinated $O^{NO_3^-} - H^{HEH^+}$ atoms within first solvation shell labelled.

arrangement of HEHN cations and anions within the bulk. The HA^+ cation shows one distinct lobe near the hydroxyl group and three, distinct circular lobes around the ammonium group. Based on the force field parameterization conducted for this study, the torsion about the N−O bond has a barrier height of approximately 1.1 kcal mol^{-1}, thus explaining the multi-directional N_1-H_{2-4} O_1 H-bonding with the HA^+ cation. The sampled configuration of the HAN−HEHN system is shown in Figure 16.

H-Bonding Analysis. The RDF, ADF, and SDFs discussed above provide a complete picture of the X−H···Y H-bonding
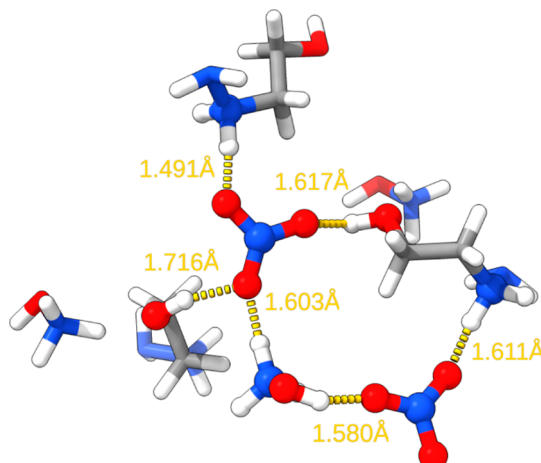
Figure 16. Representative geometry of bulk-phase 50−50% HAN-HEHN mixture within the first solvation shell.

of the studied HAN−HEHN systems. As described earlier, the hydrogen−acceptor distance combined with the donor−hydrogen−acceptor angle provides geometric criteria and a means of classifying the H-bond type.[134] Because the ADF alone may not be averaged over all possible separations, combined distribution functions (CDFs) of both RDFs and ADFs elucidate the coordination environment more precisely,[140] as shown in Figure 17.

Each CDF features a rectangle to emphasize the region of highest propensity to H-bonding for either amine- (Figure 17a and 17c) or hydroxyl-based (Figure 17b and 17d) donors. Horizontally, this dense region spans the first solvation shell according to r_{min} values of the 50−50% HAN−HEHN mixture from Table 3; vertically, the approximate angle from the saddle point to an approximate normalized occurrence value of 0.5. Per many common literature criteria,[134,141] both N−H···O and O−H···O H-bonds studied in this work classify as "moderately" strong "ionic" H-bonds, as expected. However, the resulting rectangles unambiguously highlight a stark contrast, where hydroxyl-based donors allow a greater occurrence of nonlinear H-bonds (between ∼150 and 180°) as opposed to amine-based H-bonds (between 160 and 180°). PILs demonstrating similar nanostructural signatures[142] indicate that the prevalence of strong, linear H-bonding leads to more "solid-like" physical properties (e.g., decreased ion mobility, increased viscosity) that are central to the operation of HAN−HEHN mixtures use as a propellant.

Moreover, H-bonding is transient in nature.[143] To facilitate the geometric understanding provided in Figure 17, the hydrogen bond lifetimes are calculated using the reactive flux method[144] implemented in Travis.[131] This is completed by fitting the H-bond correlation function, $c(t)$, and the local strain in the H-bond network, $n(t)$, in the given kinetic equation

$$-\dot{c}(t) = k_d c(t) - k_f n(t) \qquad (5)$$

The forward (breaking) and backward (reformation) rate constants, k_d and k_f, respectively, provide the average hydrogen bond lifetime, $\tau^{HB} = 1/k_d$, and the H-bond reformation time, $\tau^{HB} = 1/k_d$. The H-bond analysis was performed on a per-hydrogen atom basis using the rectangular criteria demarcated in Figure 17.

The average H-bond and reformation times are provided in Table 4. Because lifetime calculations are sensitive to temperature, the 50−50% HAN−HEHN mixture computed at 293 K, a slightly lower "room temperature" (necessary for direct comparison with experimental density), was omitted. The lifetimes observed for HAN and HEHN H-bonds are generally 2 to 3 orders of magnitude larger than aprotic IL counterparts.[143,145] This is expected given the accepted "solid-like" behavior of PILs with predominantly strong, linear H-bonds that limit fluid-like mobility.[142] Compared to hydroxyl-based H-bonds, the amine-based lifetimes are the longest; this result is consistent with the conclusions from the structural properties presented earlier, where the N_1 hydrogens require shorter and more linear H-bonds. Moreover, increased HAN mole fraction reduces H-bond lifetimes across all H-bond types. This is explained by the overall weakening of the H-bond network due to the increased competition and accessibility of H-bonding donor/acceptor sites. Interestingly, the HA^+ H-bond lifetimes are shorter than HEH^+, even at the highest χ_{HAN}. This is likely due to the HA^+ having one more hydrogen than HEH^+ that is actively participating in the overall
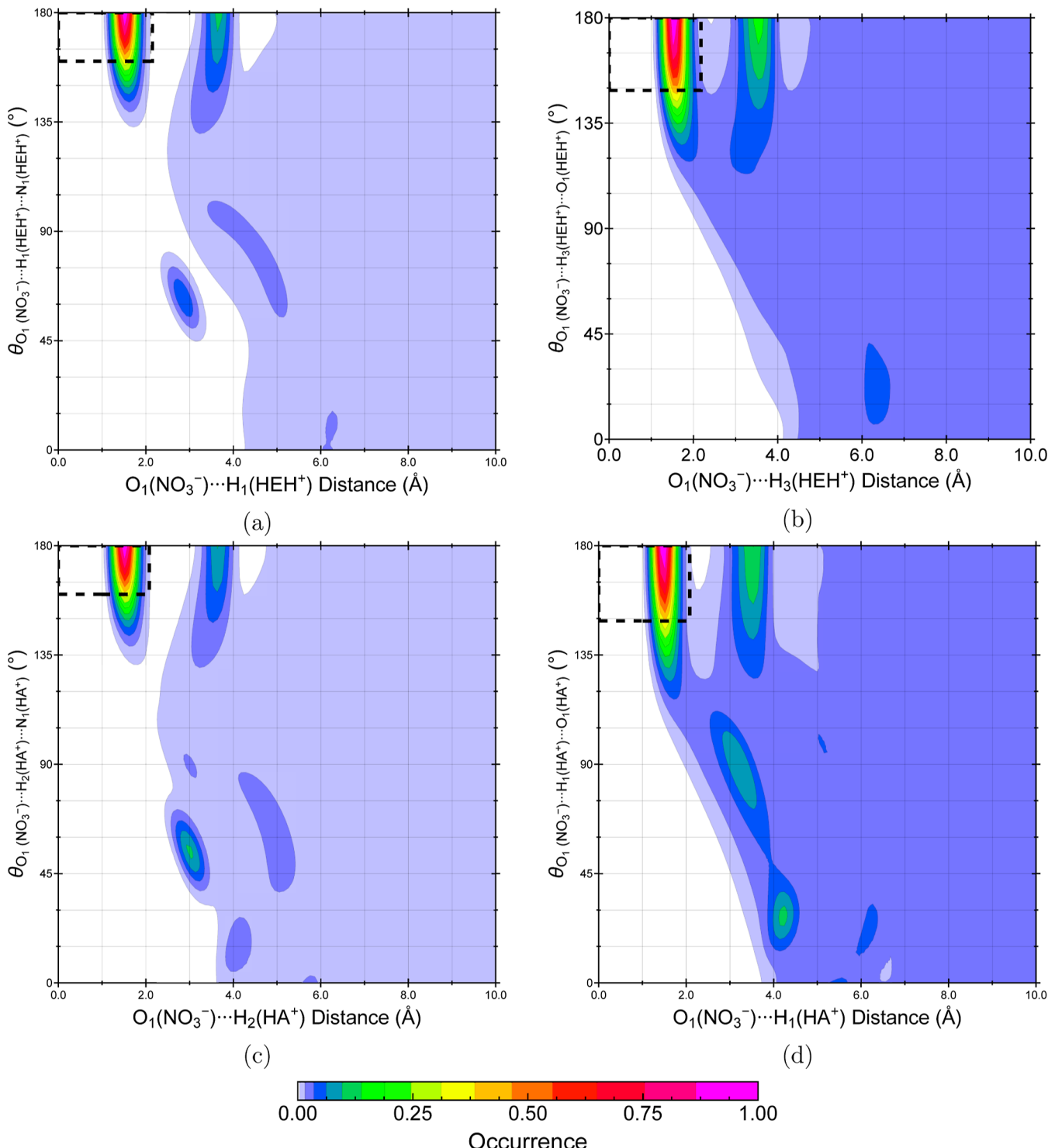
Figure 17. CDFs of O⋯H RDFs and O⋯H⋯N (left column) or O⋯H⋯O (right column) ADFs for the bulk-phase 50−50% HAN-HEHN mixture.

H-bonding network, thereby shortening its interaction per acceptor.

Multimode Propulsion Propellant Implications. As mentioned in the Introduction, while space mission flexibility or adaptability are notable advantages for MMP,[81] granular-level engineering tradeoffs require complete knowledge of key properties that influence performance. Experimental investigations of such properties for standalone propellants are limited, let alone for binary mixtures. Thus, the computational

results presented in this work contribute toward a much desired, comprehensive database of chemical properties for HAN- and HEHN-based propellants needed to accelerate MMP technologies.

One trade-off often considered is the mass savings associated with various propellants. For example, AF-M315E, the EIL blend predominantly composed of HAN, HEHN, and water, has a 50% greater density specific impulse ($\rho I_{sp} \approx 367\,500$ kg s m^{-3}) than hydrazine ($\rho I_{sp} \approx 240\,000$ kg s m^{-3});[66]

Table 4. Hydrogen Bond Lifetimes (τ_{lt}^{HB}) and Reformation Times (τ_{ft}^{HB}) in HEHN and HAN−HEHN Mixtures at 298 K from Reactive Flux Analysis (τ Values Reported in ps)^a

cation	H-bond donor	$\chi_{HAN} = 0.0$		$\chi_{HAN} = 0.326$		$\chi_{HAN} = 0.812$	
		τ_{lt}^{HB}	τ_{ft}^{HB}	τ_{lt}^{HB}	τ_{ft}^{HB}	τ_{lt}^{HB}	τ_{ft}^{HB}
HA$^+$	N$_1$			1701.9	2416.7	649.7	1375.1
	O$_1$			652.8	350.4	316.2	248.7
HEH$^+$	N$_1$	4822.0	993.7	3141.5	1020.9	1812.2	1048.6
	O$_1$	903.5	162.3	921.3	151.8	553.5	276.9

^{a}H-bond acceptor was set to $O_1^{NO_3^-}$.
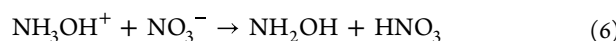
consequently, the per-volume performance of HAN and HEHN-based mixtures is advantageous and can reduce the required mass for propellant storage (i.e., tank mass).[81] As quantified in Figure 3, the increase in density from "neat" HEHN to 50−50% HAN−HEHN, 1.391 g cm^{-3} (298 K) to 1.518 g cm^{-3} (293 K), respectively, shows that HEHN and HAN complement each other not only functionally as chemical fuel and oxidizer components, respectively, but also as structural counterparts to balance the molecular volume and bulkiness of HEHN with the compactness of HAN for an overall denser mixture. Figure 4 is equally as important since a linear approximation would poorly predict the increase in density as a function of χ_{HAN}. However, the synthesis of purely HAN−HEHN mixtures may be faced with practical challenges (e.g., phase separation) due to their non-ideal mixing behavior as indicated by large, positive excess molar volumes in Figure 5. In future work, we will explore the influence of water on miscibility for binary or tertiary mixtures with HAN and HEHN.

Moreover, technologies most relevant to MMP, such as chemical or electric thrusters, depend on macroscopic properties that are fundamentally dependent on the bulk-phase ion structure. For instance, as mentioned in the Introduction, electrospray performance depends on the distribution of emitted species, which to reduced order, is dependent upon surface tension, conductivity, and viscosity.[82] While explicit calculations of transport properties shall be presented in subsequent work, insights from short- and long-range structural ordering are essential to seeking a fundamental understanding of dynamics and how they can be tuned.[142] In analyzing the electrostatics of the neat HEHN and HAN−HEHN system by the charge sum rules, the anti-correlated charge oscillations in Figure 7 illustrate the "disordered lattice" as described by Roy et al.[146] This favorable cation−anion packing along with the strong cohesive energies associated with their Coulombic interactions manifests macroscopically in the form of overall high viscosity and slow ion mobility.[107] This "resistance" to structural rearrangement further highlights the importance of radial, angular, and SDFs presented earlier. The strong signatures of H-bonding from our structural analysis corroborate the hypothesis of longer transport time scales and will require more demanding computational simulations.

Lastly, for thrusters that involve electrochemical or catalytic decomposition, the prediction of performance requires knowledge of intermediate propellant breakdown mechanisms, kinetic rate coefficients, and plume species composition. Reactive bulk-phase systems may undergo proton hopping (cf. Grothuss mechanisms) that perturb H-bond networks and ion transport.[147,148] Moreover, previous MD simulations show that ILs' response to external electric fields may induce a wider range of possible breakdown mechanisms, from evaporation to

fission, that are especially relevant to understanding electrospray thrusters.[110,111,149−152] Consequently, the geometric conditions and stability of H-bonding from Figure 17 and Table 4 serve as essential prerequisites toward developing accurate reactive force fields[153] which, in turn, inform parameters in many reduced-order thruster performance models.[154−157]

It is worth noting that the H-bonds described thus far have been classified based on their coordination length and directionality. However, H-bonding is typically considered to be a "point along the proton transfer coordinate",[134] a criterion that nonreactive simulations are unable to address. While H-bonding has been reported for various PILs in the literature,[129,134,142] the complex reaction chemistry of HAN and HEHN has been hardly studied for bulk phase systems. Nonetheless, both experimental and theoretical insights indicate that the first step in the decomposition mechanism for HAN and HEHN are eqs 6 and 7, respectively[154,158]

$$NH_3OH^+ + NO_3^- \rightarrow NH_2OH + HNO_3 \tag{6}$$

$$HEHN \rightarrow HEH + HNO_3 \tag{7}$$

Recent theoretical studies of neutral, gas-phase complexes[23,159] and small solvated clusters[96,104,136] support the hypotheses that these proton transfer reactions occur at the ammonium group via one of three N$_1$−H···O H-bonds in HAN and via the N$_1$−H···O H-bonds in HEHN. However, as both Patrick et al.[96] and Zeng et al.[136] point out, local charge distribution is heavily influenced by the surrounding medium—larger cluster sizes consistently showed less pronounced proton mobility due to "microsolvation" effects (or more commonly, "solvent effects"[160]). Finally, the different behaviors of HAN and HEHN electrosprays recently observed by Zhou and co-worker[104,161] may be explained through the nature of their respective H-bonding networks that provide a mechanism for proton transfer.

CONCLUSIONS

Molecular dynamics simulations using the APPLE&P polarizable force field were conducted to investigate the interplay between cations and anions and their influence on the bulk thermophysical properties and structure at varied mole fractions of HAN when mixed with HEHN. The temperature-dependent density was in agreement with existing literature values and the excess molar volume curves were consistent with trends found for various double salt IL mixtures. Moreover, the fundamental structural properties were found to manifest at both long- and short-range length scales. Like molten salts in general, HAN−HEHN mixtures follow long-range electroneutrality based on anti-correlated charge oscillation patterns of cations and anions out past 15 Å.

Conversely, within a first solvation shell of approximately 2 Å, HEH$^+$ and HA$^+$ cations experience strong and linear N−H···O hydrogen bonds.

The radial, angular, and SDFs showed a clear description of the competition amongst several possible hydrogen bond donor/acceptor sites. For instance, while the RDFs suggest strong connectivity among the O−H···O hydrogen bonds, their broad angular distributions indicate more flexible H-bonds that deviate from a predominantly linear arrangement with the lone pair orbital of the nitrate anions. H-bonding competition results in highly localized rearrangement, yielding favorable, cation−cation structural motifs as well.

As described in the Introduction, mixtures containing HEHN and HAN show great promise as possible MMP propellants. The presented results have far-reaching engineering implications for the selection, synthesis, and ultimately, performance of HAN−HEHN-based MMP propellants. Categorically, they are regarded as protic ILs and thereby necessitate a complete understanding of the chemical kinetics of relevant proton transfer behavior. While this work elucidates the nonreactive, statistical nature of hydrogen bonding, future work in reactive simulations is needed to fully explore the initial proton transfer aided by hydrogen-bonded complexes before and after a suitable transition state involved in the bulk phase, decomposition reaction coordinate.

ASSOCIATED CONTENT

Supporting Information

The Supporting Information is available free of charge at https://pubs.acs.org/doi/10.1021/acs.jpcb.3c02649.

> Polarizable force field equation and basic description; Gaussian distribution for exemplar density calculations; tabulated uncertainties for all calculated densities as a function of temperature and concentration; concentration dependence for density as a function of χ_{HEHN}; excess molar volume plot with additional experimental comparisons; and peak heights from Figure 9 (PDF)

AUTHOR INFORMATION

Corresponding Author

Ghanshyam L. Vaghjiani − *AFRL/RQRS, Edwards AFB, California 93524, United States;* orcid.org/0000-0001-7473-7388; Email: ghanshyam.vaghjiani@spaceforce.mil

Authors

Shehan M. Parmar − *Department of Chemistry and Biochemistry, Georgia Institute of Technology, Atlanta, Georgia 30332, United States*

Daniel D. Depew − *Department of Astronautical Engineering, University of Southern California, Los Angeles, California 90089, United States*

Richard E. Wirz − *Department of Mechanical and Aerospace Engineering, University of California, Los Angeles, Los Angeles, California 90095, United States*

Complete contact information is available at:
https://pubs.acs.org/10.1021/acs.jpcb.3c02649

Notes

The authors declare no competing financial interest.

REFERENCES

(1) Kilpeläinen, I.; Xie, H.; King, A.; Granstrom, M.; Heikkinen, S.; Argyropoulos, D. S. Dissolution of Wood in Ionic Liquids. *J. Agric. Food Chem.* **2007**, *55*, 9142−9148.

(2) Zhang, Z.; Song, J.; Han, B. Catalytic Transformation of Lignocellulose into Chemicals and Fuel Products in Ionic Liquids. *Chem. Rev.* **2017**, *117*, 6834−6880.

(3) Brandt, A.; Gräsvik, J.; Hallett, J. P.; Welton, T. Deconstruction of lignocellulosic biomass with ionic liquids. *Green Chem.* **2013**, *15*, 550−583.

(4) Ye, C.; Liu, W.; Chen, Y.; Yu, L. Room-temperature ionic liquids: a novel versatile lubricant. *Chem. Commun.* **2001**, 2244−2245.

(5) Liu, W.; Ye, C.; Gong, Q.; Wang, H.; Wang, P. Tribological Performance of Room-Temperature Ionic Liquids as Lubricant. *Tribol. Lett.* **2002**, *13*, 81−85.

(6) Sun, X.; Luo, H.; Dai, S. Ionic Liquids-Based Extraction: A Promising Strategy for the Advanced Nuclear Fuel Cycle. *Chem. Rev.* **2012**, *112*, 2100−2128.

(7) Anthony, J. L.; Anderson, J. L.; Maginn, E. J.; Brennecke, J. F. Anion Effects on Gas Solubility in Ionic Liquids. *J. Phys. Chem. B* **2005**, *109*, 6366−6374.

(8) Lei, Z.; Dai, C.; Chen, B. Gas Solubility in Ionic Liquids. *Chem. Rev.* **2014**, *114*, 1289−1326.

(9) Zeng, S.; Zhang, X.; Bai, L.; Zhang, X.; Wang, H.; Wang, J.; Bao, D.; Li, M.; Liu, X.; Zhang, S. Ionic-Liquid-Based CO2 Capture Systems: Structure, Interaction and Process. *Chem. Rev.* **2017**, *117*, 9625−9673.

(10) Wang, S.; Wang, X. Imidazolium Ionic Liquids, Imidazolylidene Heterocyclic Carbenes, and Zeolitic Imidazolate Frameworks for CO2 Capture and Photochemical Reduction. *Angew. Chem., Int. Ed.* **2016**, *55*, 2308−2320.

(11) Shukla, S. K.; Khokarale, S. G.; Bui, T. Q.; Mikkola, J.-P. T. Ionic Liquids: Potential Materials for Carbon Dioxide Capture and Utilization. *Front. Mater.* **2019**, *6*, 1−8.

(12) Zhang, Q.; Wang, Q.; Zhang, S.; Lu, X.; Zhang, X. Electrodeposition in Ionic Liquids. *ChemPhysChem* **2016**, *17*, 335−351.

(13) MacFarlane, D. R.; Tachikawa, N.; Forsyth, M.; Pringle, J. M.; Howlett, P. C.; Elliott, G. D.; Davis, J. H.; Watanabe, M.; Simon, P.; Angell, C. A. Energy applications of ionic liquids. *Energy Environ. Sci.* **2014**, *7*, 232−250.

(14) Balducci, A. Ionic Liquids in Lithium-Ion Batteries. *Top. Curr. Chem.* **2017**, *375*, 20.

(15) Navarra, M. A. Ionic liquids as safe electrolyte components for Li-metal and Li-ion batteries. *MRS Bull.* **2013**, *38*, 548−553.

(16) Watanabe, M.; Thomas, M. L.; Zhang, S.; Ueno, K.; Yasuda, T.; Dokko, K. Application of Ionic Liquids to Energy Storage and Conversion Materials and Devices. *Chem. Rev.* **2017**, *117*, 7190−7239.

(17) Zhang, K.; Thynell, S. T. Thermal Decomposition Mechanism of Aqueous Hydroxylammonium Nitrate (HAN): Molecular Simulation and Kinetic Modeling. *J. Phys. Chem. A* **2018**, *122*, 8086−8100.

(18) Khare, P.; Yang, V.; Meng, H.; Risha, G. A.; Yetter, R. A. Thermal and Electrolytic Decomposition and Ignition of HAN-Water Solutions. *Combust. Sci. Technol.* **2015**, *187*, 1065−1078.

(19) Esparza, A. A.; Ferguson, R. E.; Choudhuri, A.; Love, N. D.; Shafirovich, E. Thermoanalytical studies on the thermal and catalytic decomposition of aqueous hydroxylammonium nitrate solution. *Combust. Flame* **2018**, *193*, 417−423.

(20) Depew, D. D.; Wang, J.; Parmar, S.; Chambreau, S.; Bedrov, D.; van Duin, A.; Vaghjiani, G. AIAA Propulsion and Energy 2019 Forum. In *AIAA Propulsion and Energy Forum*; American Institute of Aeronautics and Astronautics, 2019.

(21) Hwang, C. H.; Lee, S. N.; Baek, S. W.; Han, C. Y.; Kim, S. K.; Yu, M. J. Effects of Catalyst Bed Failure on Thermochemical Phenomena for a Hydrazine Monopropellant Thruster Using Ir/Al2O3 Catalysts. *Ind. Eng. Chem. Res.* **2012**, *51*, 5382−5393.

(22) Chambreau, S. D.; Popolan-Vaida, D. M.; Vaghjiani, G. L.; Leone, S. R. Catalytic Decomposition of Hydroxylammonium Nitrate Ionic Liquid: Enhancement of NO Formation. *J. Phys. Chem. Lett.* **2017**, *8*, 2126−2130.

(23) Chambreau, S. D.; Popolan-Vaida, D. M.; Kostko, O.; Lee, J. K.; Zhou, Z.; Brown, T. A.; Jones, P.; Shao, K.; Zhang, J.; Vaghjiani, G. L.; Zare, R. N.; Leone, S. R. Thermal and Catalytic Decomposition of 2-Hydroxyethylhydrazine and 2-Hydroxyethylhydrazinium Nitrate Ionic Liquid. *J. Phys. Chem. A* **2022**, *126*, 373−394.

(24) Terhune, K. J.; King, L. B.; He, K.; Cumings, J. Radiation-induced solidification of ionic liquid under extreme electric field. *Nanotechnology* **2016**, *27*, 375701.

(25) Iribarne, J. V.; Thomson, B. A. On the evaporation of small ions from charged droplets. *J. Chem. Phys.* **1976**, *64*, 2287−2294.

(26) Gamero-Castaño, M.; Fernández de la Mora, J. Direct measurement of ion evaporation kinetics from electrified liquid surfaces. *J. Chem. Phys.* **2000**, *113*, 815−832.

(27) Gu, W.; Heil, P. E.; Choi, H.; Kim, K. Comprehensive model for fine Coulomb fission of liquid droplets charged to Rayleigh limit. *Appl. Phys. Lett.* **2007**, *91*, 64104.

(28) Gomez, A.; Deng, W. *Aerosol Measurement*; Wiley Online Books, 2011; Chapter 20, pp 435−448.

(29) Thuppul, A.; Wright, P. L.; Collins, A. L.; Ziemer, J. K.; Wirz, R. E. Lifetime Considerations for Electrospray Thrusters. *Aerospace* **2020**, *7*, 108.

(30) Schmidt, E. W. E. W. *Hydrazine and its derivatives : preparation, properties, applications*; John Wiley & Sons: New York, 1984l p 1059.

(31) Sawyer, R. F.; Glassman, I. Gas-phase reactions of hydrazine with nitrogen dioxide, nitric oxide, and oxygen. *Symp. (Int.) Combust.* **1967**, *11*, 861−869.

(32) Schmidt, M. W.; Gordon, M. S. The Decomposition of Hydrazine in the Gas Phase and over an Iridium Catalyst. *Z. Phys. Chem.* **2013**, *227*, 1301−1336.

(33) Price, T. W.; Evans, D. D. The Status of Monopropellant Hydrazine Technology. 1968, https://ntrs.nasa.gov/citations/19680006875 (accessed on April 21, 2023).

(34) Wood, S. E.; Bryant, J. T. Decomposition of Hydrazine on Shell 405 Catalyst at High Presure. *Prod. R&D* **1973**, *12*, 117−122.

(35) Agency for Toxic Substances and Disease Registry (ATSDR). Toxicological Profile for Hydrazines. 1997, https://www.atsdr.cdc.gov/ToxProfiles/tp100.pdf (accessed on April 21, 2023).

(36) Nosseir, A. E.; Cervone, A.; Pasini, A. Review of state-of-the-art green monopropellants: For propulsion systems analysts and designers. *Aerospace* **2021**, *8*, 20.

(37) Schneider, S.; Hawkins, T.; Rosander, M.; Vaghjiani, G.; Chambreau, S.; Drake, G. Ionic Liquids as Hypergolic Fuels. *Energy Fuels* **2008**, *22*, 2871−2872.

(38) Sebastiao, E.; Cook, C.; Hu, A.; Murugesu, M. Recent developments in the field of energetic ionic liquids. *J. Mater. Chem. A* **2014**, *2*, 8153−8173.

(39) Gao, A.; Oyumi, Y.; Brill, T. B. Thermal decomposition of energetic materials 49. Thermolysis routes of mono- and diaminotetrazoles. *Combust. Flame* **1991**, *83*, 345−352.

(40) Lesnikovich, A. I.; Ivashkevich, O. A.; Levchik, S. V.; Balabanovich, A. I.; Gaponik, P. N.; Kulak, A. A. Thermal decomposition of aminotetrazoles. *Thermochim. Acta* **2002**, *388*, 233−251.

(41) Gálvez-Ruiz, J. C.; Holl, G.; Karaghiosoff, K.; Klapötke, T. M.; Löhnwitz, K.; Mayer, P.; Nöth, H.; Polborn, K.; Rohbogner, C. J.; Suter, M.; et al. Derivatives of 1,5-Diamino-1H-tetrazole: A New Family of Energetic Heterocyclic-Based Salts. *Inorg. Chem.* **2005**, *44*, 4237−4253.

(42) Schneider, S.; Hawkins, T.; Rosander, M.; Mills, J.; Brand, A.; Hudgens, L.; Warmoth, G.; Vij, A. Liquid Azide Salts. *Inorg. Chem.* **2008**, *47*, 3617−3624.

(43) Lin, Q.-H.; Li, Y.-C.; Li, Y.-Y.; Wang, Z.; Liu, W.; Qi, C.; Pang, S.-P. Energetic salts based on 1-amino-1,2,3-triazole and 3-methyl-1-amino-1,2,3-triazole. *J. Mater. Chem.* **2012**, *22*, 666−674.

(44) Zhang, Y.; Gao, H.; Guo, Y.; Joo, Y.-H.; Shreeve, J. M. Hypergolic, N. HypergolicN,N-Dimethylhydrazinium Ionic Liquids. *Chem.—Eur. J.* **2010**, *16*, 3114−3120.

(45) Smiglak, M.; Hines, C. C.; Wilson, T. B.; Singh, S.; Vincek, A. S.; Kirichenko, K.; Katritzky, A. R.; Rogers, R. D. Ionic Liquids Based on Azolate Anions. *Chem.—Eur. J.* **2010**, *16*, 1572−1584.

(46) Joo, Y.-H.; Gao, H.; Zhang, Y.; Shreeve, J. M. Inorganic or Organic Azide-Containing Hypergolic Ionic Liquids⊥⊥ As poster published in 1st Korean International Symposium on High Energy Materials, Incheon, Korea, October 6−9, 2009. *Inorg. Chem.* **2010**, *49*, 3282−3288.

(47) Habereder, T.; Hammerl, A.; Holl, G.; Klapötke, T. M.; Knizek, J.; Nöth, H. Synthesis and X-ray Structure Determination of tert-Butylhydrazinium Azide and N,N,N-Trimethylhydrazinium Azide. *Eur. J. Inorg. Chem.* **1999**, *1999*, 849−852.

(48) Hammerl, A.; Holl, G.; Kaiser, M.; Klapötke, T. M.; Mayer, P.; Nöth, H.; Warchhold, M. New Hydrazinium Azide Compounds. *Z. Anorg. Allg. Chem.* **2001**, *627*, 1477−1482.

(49) Hammerl, A.; Holl, G.; Kaiser, M.; Klapötke, T. M.; Kränzle, R.; Vogt, M. N,N-Diorganylsubstituted Hydrazinium Azides. *Z. Anorg. Allg. Chem.* **2002**, *628*, 322−325.

(50) Gao, Y.; Gao, H.; Piekarski, C.; Shreeve, J. M. Azolium Salts Functionalized with Cyanomethyl, Vinyl, or Propargyl Substituents and Dicyanamide, Dinitramide, Perchlorate and Nitrate Anions. *Eur. J. Inorg. Chem.* **2007**, *2007*, 4965−4972.

(51) Zhang, Y.; Shreeve, J. M. Dicyanoborate-Based Ionic Liquids as Hypergolic Fluids. *Angew. Chem., Int. Ed.* **2011**, *50*, 935−937.

(52) Drab, D. M.; Smiglak, M.; Shamshina, J. L.; Kelley, S. P.; Schneider, S.; Hawkins, T. W.; Rogers, R. D. Synthesis of N-cyanoalkyl-functionalized imidazolium nitrate and dicyanamide ionic liquids with a comparison of their thermal properties for energetic applications. *New J. Chem.* **2011**, *35*, 1701−1717.

(53) Sabaté, C. M.; Delalu, H. Energetic Salts of Symmetrical Dimethylhydrazine (SDMH). *Eur. J. Inorg. Chem.* **2012**, *2012*, 866−877.

(54) Isaac Sam, I.; Gayathri, S.; Santhosh, G.; Cyriac, J.; Reshmi, S. Exploring the possibilities of energetic ionic liquids as non-toxic hypergolic bipropellants in liquid rocket engines. *J. Mol. Liq.* **2022**, *350*, 118217.

(55) Igarashi, S.; Matsuura, Y. 53rd AIAA/SAE/ASEE Joint Propulsion Conference. *AIAA Propulsion and Energy Forum*; American Institute of Aeronautics and Astronautics, 2017.

(56) Igarashi, S.; Matsuura, Y.; Ikeda, H.; Hatai, K. AIAA Propulsion and Energy 2019 Forum. In *AIAA Propulsion and Energy Forum*; American Institute of Aeronautics and Astronautics, 2019.

(57) Hooper, J. B.; Borodin, O.; Schneider, S. Insight into Hydrazinium Nitrates, Azides, Dicyanamide, and 5-Azidotetrazolate Ionic Materials from Simulations and Experiments. *J. Phys. Chem. B* **2011**, *115*, 13578−13592.

(58) Negri, M.; Wilhelm, M.; Hendrich, C.; Wingborg, N.; Gediminas, L.; Adelöw, L.; Maleix, C.; Chabernaud, P.; Brahmi, R.;

Beauchet, R.; et al. New technologies for ammonium dinitramide based monopropellant thrusters − The project RHEFORM. *Acta Astronaut.* **2018**, *143*, 105−117.

(59) Thakre, P.; Duan, Y.; Yang, V. Modeling of ammonium dinitramide (ADN) monopropellant combustion with coupled condensed and gas phase kinetics. *Combust. Flame* **2014**, *161*, 347−362.

(60) Wada, A.; Habu, H. Electric Ignition Characteristics of an Ammonium-Dinitramide-Based Ionic Liquid Monopropellant with Discharge Plasma. In *AIAA SciTech Forum*; American Institute of Aeronautics and Astronautics, 2020.

(61) Klein, N. Liquid Propellants For Use in Guns—A Review. 1985, https://apps.dtic.mil/sti/pdfs/ADA153051.pdf (accessed on April 21, 2023).

(62) Schmidt, E. W. Hydroxylammonium Nitrate Compatibility Tests with Various Materials—A Liquid Propellant Study. 1990, https://apps.dtic.mil/sti/pdfs/ADA224594.pdf (accessed on April 21, 2023).

(63) Amrousse, R.; Katsumi, T.; Bachar, A.; Brahmi, R.; Bensitel, M.; Hori, K. Chemical engineering study for hydroxylammonium nitrate monopropellant decomposition over monolith and grain metal-based catalysts. *React. Kinet., Mech. Catal.* **2014**, *111*, 71−88.

(64) Farhat, K.; Batonneau, Y.; Florea, O.; Kappenstein, C.; Ford, M. 42nd AIAA/ASME/SAE/ASEE Joint Propulsion Conference & Exhibit. In *Joint Propulsion Conferences*; American Institute of Aeronautics and Astronautics, 2006.

(65) Swami, U.; Senapathi, K.; Srinivasulu, K. M.; Desingu, J.; Chowdhury, A. Ignition Delays of Mixtures of the Non-Hypergolic Energetic Ionic Liquid Hydroxyethylhydrazinium Nitrate Blended with Unsymmetrical Dimethylhydrazine. *Propellants, Explos., Pyrotech.* **2019**, *44*, 1139−1146.

(66) Freudenmann, D.; Ciezki, H. K. ADN and HAN-Based Monopropellants − A Minireview on Compatibility and Chemical Stability in Aqueous Media. *Propellants, Explos., Pyrotech.* **2019**, *44*, 1084−1089.

(67) Persson, M.; Anflo, K.; Friedhoff, P. Flight Heritage of Ammonium Dinitramide (ADN) Based High Performance Green Propulsion (HPGP) Systems. *Propellants, Explos., Pyrotech.* **2019**, *44*, 1073−1079.

(68) Wilhelm, M.; Negri, M.; Ciezki, H.; Schlechtriem, S. Preliminary tests on thermal ignition of ADN-based liquid monopropellants. *Acta Astronaut.* **2019**, *158*, 388−396.

(69) Decker, M. M.; Klein, N.; Freedman, E.; Leveritt, C. S.; Wojciechowski, J. Q. HAN-based Liquid Gun Propellants: Physical Properties. 1987, https://apps.dtic.mil/sti/citations/ADA195246 (accessed on April 21, 2023).

(70) Hansen, R.; Backof, E.; De Grieff, H. J.; Klein, N. *Processes for Assessing the Thermal Stability of Han-Based Liquid Propellants: Final Report*, 1990, https://www.dtic.mil/docs/citations/ADA224999 (accessed on April 21, 2023).

(71) Klein, N.; Baer, P. G. The Effects of Composition Variation and Nitric Acid on the Stability and Reactivity of the Han-Based Liquid Propellants. 1991, https://apps.dtic.mil/sti/pdfs/ADA231502.pdf (accessed on April 21, 2023).

(72) Masse, R.; Overly, J.; Allen, M.; Spores, R. 48th AIAA/ASME/SAE/ASEE Joint Propulsion Conference & Exhibit. *Joint Propulsion Conferences*; American Institute of Aeronautics and Astronautics, 2012.

(73) Hori, K.; Katsumi, T.; Sawai, S.; Azuma, N.; Hatai, K.; Nakatsuka, J. HAN-Based Green Propellant, SHP163 − Its R&D and Test in Space. *Propellants, Explos., Pyrotech.* **2019**, *44*, 1080−1083.

(74) Thrasher, J.; Williams, S.; Takahashi, P.; Sousa, J. 52nd AIAA/SAE/ASEE Joint Propulsion Conference. In *AIAA Propulsion and Energy Forum*; American Institute of Aeronautics and Astronautics, 2016.

(75) Goebel, D. M.; Katz, I. *Fundamentals of Electric Propulsion: Ion and Hall Thrusters*; Jet Propulsion Laboratory, California Institute of Technology, 2008;p 486.

(76) Wirz, R.; Mueller, J.; Gale, M.; Marrese, C. 40th AIAA/ASME/SAE/ASEE Joint Propulsion Conference and Exhibit. *Joint Propulsion Conferences*; American Institute of Aeronautics and Astronautics, 2004.

(77) Gamero-Castaño, M. The structure of electrospray beams in vacuum. *J. Fluid Mech.* **2008**, *604*, 339−368.

(78) Ziemer, J.; Gamero-Castaño, M.; Hruby, V.; Spence, D.; Demmons, N.; McCormick, R.; Roy, T.; Gasdaska, C.; Young, J.; Connolly, B. Colloid Micro-Newton Thruster Development for the ST7-DRS and LISA Missions. In *41st AIAA/ASME/SAE/ASEE Joint Propulsion Conference & Exhibit: Tucson, Arizona*, 2005.

(79) Lozano, P. C. Energy properties of an EMI-Im ionic liquid ion source. *J. Phys. D: Appl. Phys.* **2005**, *39*, 126−134.

(80) Wainwright, M. J. Experimental investigation of ionic liquid mixtures for electrospray propulsion. Ph.D. Thesis, Missouri University of Science and Technology, 2020.

(81) Rovey, J. L.; Lyne, C. T.; Mundahl, A. J.; Rasmont, N.; Glascock, M. S.; Wainwright, M. J.; Berg, S. P. Review of multimode space propulsion. *Prog. Aero. Sci.* **2020**, *118*, 100627.

(82) Prince, B. D.; Fritz, B. A.; Chiu, Y.-H.. In *Ionic Liquids: Science and Applications*; ACS Symposium Series; American Chemical Society, 2012; Vol. *1117*, pp 2−27.

(83) Hollóczki, O.; Gerhard, D.; Massone, K.; Szarvas, L.; Németh, B.; Veszprémi, T.; Nyulászi, L. Carbenes in ionic liquids. *New J. Chem.* **2010**, *34*, 3004−3009.

(84) De Vos, N.; Maton, C.; Stevens, C. V. Electrochemical Stability of Ionic Liquids: General Influences and Degradation Mechanisms. *ChemElectroChem* **2014**, *1*, 1258−1270.

(85) Wooster, T. J.; Johanson, K. M.; Fraser, K. J.; MacFarlane, D. R.; Scott, J. L. Thermal degradation of cyano containing ionic liquids. *Green Chem.* **2006**, *8*, 691−696.

(86) Chingin, K.; Perry, R. H.; Chambreau, S. D.; Vaghjiani, G. L.; Zare, R. N. Generation of melamine polymer condensates upon hypergolic ignition of dicyanamide ionic liquids. *Angew. Chem., Int. Ed. Engl.* **2011**, *50*, 8634−8637.

(87) Chambreau, S. D.; Schenk, A. C.; Sheppard, A. J.; Yandek, G. R.; Vaghjiani, G. L.; Maciejewski, J.; Koh, C. J.; Golan, A.; Leone, S. R. Thermal Decomposition Mechanisms of Alkylimidazolium Ionic Liquids with Cyano-Functionalized Anions. *J. Phys. Chem. A* **2014**, *118*, 11119−11132.

(88) Donius, B. R.; Rovey, J. L. Ionic Liquid Dual-Mode Spacecraft Propulsion Assessment. *J. Spacecr. Rockets* **2011**, *48*, 110−123.

(89) Klein, N. An Infra-Red Investigation of Han-Based Liquid Propellants, 1987 https://apps.dtic.mil/sti/citations/ADA187226 (accessed on: April 21, 2023).

(90) Rasmont, N.; Broemmelsiek, E. J.; Mundahl, A.; Rovey, J. AIAA Propulsion and Energy 2019 Forum. In *AIAA Propulsion and Energy Forum*; American Institute of Aeronautics and Astronautics, 2019.

(91) Mundahl, A. J.; Berg, S. P.; Rovey, J.; Huang, M.; Woelk, K.; Wagle, D.; Baker, G. 53rd AIAA/SAE/ASEE Joint Propulsion Conference *AIAA Propulsion and Energy Forum*; American Institute of Aeronautics and Astronautics, 2017.

(92) Chang, Y.-P.; Boyer, E.; Kuo, K. K. Combustion Behavior and Flame Structure of XM46 Liquid Propellant. *J. Propul. Power* **2001**, *17*, 800−808.

(93) Bhosale, V. K.; Jeong, J.; Kwon, S. Ignition of boron-based green hypergolic fuels with hydrogen peroxide. *Fuel* **2019**, *255*, 115729.

(94) Amrousse, R.; Katsumi, T.; Azuma, N.; Hori, K. Hydroxylammonium nitrate (HAN)-based green propellant as alternative energy resource for potential hydrazine substitution: From lab scale to pilot plant scale-up. *Combust. Flame* **2017**, *176*, 334−348.

(95) Wainwright, M. J.; Rovey, J.; Miller, S. W.; Prince, B. D.; Berg, S. P. Hydroxylammonium Nitrate Species in a Monopropellant Electrospray Plume. *AIAA Propulsion and Energy 2019 Forum*, 2019.

(96) Patrick, A. L.; Vogelhuber, K. M.; Prince, B. D.; Annesley, C. J. Theoretical and Experimental Insights into the Dissociation of 2-Hydroxyethylhydrazinium Nitrate Clusters Formed via Electrospray. *J. Phys. Chem. A* **2018**, *122*, 1960−1966.

(97) Chatel, G.; Pereira, J. F. B.; Debbeti, V.; Wang, H.; Rogers, R. D. Mixing ionic liquids − "simple mixtures" or "double salts". *Green Chem.* **2014**, *16*, 2051−2083.

(98) Larriba, M.; Navarro, P.; García, J.; Rodríguez, F. Liquid−Liquid Extraction of Toluene from n-Alkanes using {[4empy] [Tf2N] + [emim] [DCA]} Ionic Liquid Mixtures. *J. Chem. Eng. Data* **2014**, *59*, 1692−1699.

(99) Zheng, W.; Liu, X.; Zhang, J.; Cheng, Y.; Wang, W. Molecular dynamics simulation of ionic liquid electrospray: Microscopic presentation of the effects of mixed ionic liquids. *Int. J. Heat Mass Transfer* **2022**, *182*, 121983.

(100) Greaves, T. L.; Drummond, C. J. Protic Ionic Liquids: Properties and Applications. *Chem. Rev.* **2008**, *108*, 206−237.

(101) Hayes, R.; Warr, G. G.; Atkin, R. Structure and Nanostructure in Ionic Liquids. *Chem. Rev.* **2015**, *115*, 6357−6426.

(102) Alfano, A. J.; Mills, J. D.; Vaghjiani, G. L. Resonant Laser Ignition Study of HAN-HEHN Propellant Mixture. *Combust. Sci. Technol.* **2009**, *181*, 902−913.

(103) Chambreau, S. D.; Schneider, S.; Rosander, M.; Hawkins, T.; Gallegos, C. J.; Pastewait, M. F.; Vaghjiani, G. L. Fourier Transform Infrared Studies in Hypergolic Ignition of Ionic Liquids. *J. Phys. Chem. A* **2008**, *112*, 7816−7824.

(104) Zhou, W.; Liu, J.; Chambreau, S. D.; Vaghjiani, G. L. Structures, proton transfer and dissociation of hydroxylammonium nitrate (HAN) revealed by electrospray ionization tandem mass spectrometry and molecular dynamics simulations. *Phys. Chem. Chem. Phys.* **2022**, *24*, 14033−14043.

(105) Bedrov, D.; Piquemal, J.-P.; Borodin, O.; MacKerell, A. D.; Roux, B.; Schröder, C. Molecular Dynamics Simulations of Ionic Liquids and Electrolytes Using Polarizable Force Fields. *Chem. Rev.* **2019**, *119*, 7940−7995.

(106) Hooper, J. B.; Smith, G. D.; Bedrov, D. Thermophysical properties of energetic ionic liquids/nitric acid mixtures: Insights from molecular dynamics simulations. *J. Chem. Phys.* **2013**, *139*, 104503.

(107) McDaniel, J. G.; Yethiraj, A. Understanding the Properties of Ionic Liquids: Electrostatics, Structure Factors, and Their Sum Rules. *J. Phys. Chem. B* **2019**, *123*, 3499−3512.

(108) Zhong, X.; Liu, Z.; Cao, D. Improved Classical United-Atom Force Field for Imidazolium-Based Ionic Liquids: Tetrafluoroborate, Hexafluorophosphate, Methylsulfate, Trifluoromethylsulfonate, Acetate, Trifluoroacetate, and Bis(trifluoromethylsulfonyl)amide. *J. Phys. Chem. B* **2011**, *115*, 10027−10040.

(109) Sambasivarao, S. V.; Acevedo, O. Development of OPLS-AA Force Field Parameters for 68 Unique Ionic Liquids. *J. Chem. Theory Comput.* **2009**, *5*, 1038−1050.

(110) Prince, B. D.; Tiruppathi, P.; Bemish, R. J.; Chiu, Y.-H.; Maginn, E. J. Molecular Dynamics Simulations of 1-Ethyl-3-methylimidazolium Bis[(trifluoromethyl)sulfonyl]imide Clusters and Nanodrops. *J. Phys. Chem. A* **2015**, *119*, 352−368.

(111) Zhang, J.; Cai, G.; Liu, X.; He, B.; Wang, W. Molecular dynamics simulation of ionic liquid electrospray: Revealing the effects of interaction potential models. *Acta Astronaut.* **2021**, *179*, 581−593.

(112) McDaniel, J. G.; Choi, E.; Son, C. Y.; Schmidt, J. R.; Yethiraj, A. Ab Initio Force Fields for Imidazolium-Based Ionic Liquids. *J. Phys. Chem. B* **2016**, *120*, 7024−7036.

(113) Borodin, O. Polarizable Force Field Development and Molecular Dynamics Simulations of Ionic Liquids. *J. Phys. Chem. B* **2009**, *113*, 11463−11478.

(114) Borodin, O.; Smith, G. D. Structure and dynamics of N-methyl-N-propylpyrrolidinium bis(trifluoromethanesulfonyl)imide ionic liquid from molecular dynamics simulations. *J. Phys. Chem. B* **2006**, *110*, 11481−11490.

(115) Bedrov, D.; Borodin, O. Thermodynamic, dynamic, and structural properties of ionic liquids comprised of 1-butyl-3-methylimidazolium cation and nitrate, azide, or dicyanamide anions. *J. Phys. Chem. B* **2010**, *114*, 12802−12810.

(116) Allen, M. P.; Tildesley, D. J. *Computer Simulation of Liquids*, 2nd ed.; Oxford University Press: New York, NY, 2017; p 626.

(117) Frenkel, D.; Smit, B. In *Understanding Molecular Simulation: From Algorithms to Applications*, 2nd ed.; Frenkel, D., Smit, B., Eds.; Academic Press, 2002.

(118) Hawkins, T. Research and Development of Ionic Liquids at U.S. Air Force Research Laboratory Ionic Liquids R&D; U.S. Air Force Research Laboratory, 2005, https://apps.dtic.mil/sti/pdfs/ADA436093.pdf (accessed on April 21, 2023).

(119) Borodin, O. Polarizable Force Field Development and Molecular Dynamics Simulations of Ionic Liquids. *J. Phys. Chem. B* **2009**, *113*, 11463−11478.

(120) Gutowski, K. E.; Gurkan, B.; Maginn, E. J. Force field for the atomistic simulation of the properties of hydrazine, organic hydrazine derivatives, and energetic hydrazinium ionic liquids. *Pure Appl. Chem.* **2009**, *81*, 1799−1828.

(121) Sasse, R. A.; Davies, M. A.; Fifer, R. A.; Decker, M. M.; Kotlar, A. J. Density of Hydroxylammonium Nitrate Solutions. 1988, https://apps.dtic.mil/sti/pdfs/ADA201110.pdf (accessed on April 21, 2023).

(122) Klein, N. The Molecular Structure of the Han-Based Liquid Propellants. 1990, https://apps.dtic.mil/sti/pdfs/ADA226415.pdf (accessed on April 21, 2023).

(123) Anouti, M.; Vigeant, A.; Jacquemin, J.; Brigouleix, C.; Lemordant, D. Volumetric properties, viscosity and refractive index of the protic ionic liquid, pyrrolidinium octanoate, in molecular solvents. *J. Chem. Thermodyn.* **2010**, *42*, 834−845.

(124) Canongia Lopes, J. N.; Cordeiro, T. C.; Esperança, J. M. S. S.; Guedes, H. J. R.; Huq, S.; Rebelo, L. P. N.; Seddon, K. R. Deviations from Ideality in Mixtures of Two Ionic Liquids Containing a Common Ion. *J. Phys. Chem. B* **2005**, *109*, 3519−3525.

(125) Navia, P.; Troncoso, J.; Romaní, L. Excess Magnitudes for Ionic Liquid Binary Mixtures with a Common Ion. *J. Chem. Eng. Data* **2007**, *52*, 2542.

(126) Stoppa, A.; Buchner, R.; Hefter, G. How ideal are binary mixtures of room-temperature ionic liquids? *J. Mol. Liq.* **2010**, *153*, 46−51.

(127) Annat, G.; Forsyth, M.; MacFarlane, D. R. Ionic Liquid Mixtures—Variations in Physical Properties and Their Origins in Molecular Structure. *J. Phys. Chem. B* **2012**, *116*, 8251−8258.

(128) Oliveira, M. B.; Domínguez-Pérez, M.; Freire, M. G.; Llovell, F.; Cabeza, O.; Lopes-da Silva, J. A.; Vega, L. F.; Coutinho, J. A. P. Surface Tension of Binary Mixtures of 1-Alkyl-3-methylimidazolium Bis(trifluoromethylsulfonyl)imide Ionic Liquids: Experimental Measurements and Soft-SAFT Modeling. *J. Phys. Chem. B* **2012**, *116*, 12133−12141.

(129) Canongia Lopes, J. N.; Esperança, J. M. S. S.; de Ferro, A. M.; Pereiro, A. B.; Plechkova, N. V.; Rebelo, L. P. N.; Seddon, K. R.; Vázquez-Fernández, I.; Vázquez-Fernández, I. Protonic Ammonium Nitrate Ionic Liquids and Their Mixtures: Insights into Their Thermophysical Behavior. *J. Phys. Chem. B* **2016**, *120*, 2397−2406.

(130) Castejón, H. J.; Lashock, R. J. Mixtures of ionic liquids with similar molar volumes form regular solutions and obey the cross-square rules for electrolyte mixtures. *J. Mol. Liq.* **2012**, *167*, 1−4.

(131) Brehm, M.; Thomas, M.; Gehrke, S.; Kirchner, B. TRAVIS—A free analyzer for trajectories from molecular simulation. *J. Chem. Phys.* **2020**, *152*, 164105.

(132) Hansen, J. P.; McDonald, I. R. Statistical mechanics of dense ionized matter. IV. Density and charge fluctuations in a simple molten salt. *Phys. Rev. A: At., Mol., Opt. Phys.* **1975**, *11*, 2111−2123.

(133) Hansen, J.-P.; McDonald, I. R. B. T. *Theory of Simple Liquids*, 4th ed.; Academic Press: Oxford, U.K., 2013.

(134) Hunt, P. A.; Ashworth, C. R.; Matthews, R. P. Hydrogen bonding in ionic liquids. *Chem. Soc. Rev.* **2015**, *44*, 1257−1288.

(135) Wu, Y.; Chen, H.; Wang, F.; Paesani, F.; Voth, G. A. An Improved Multistate Empirical Valence Bond Model for Aqueous Proton Solvation and Transport. *J. Phys. Chem. B* **2008**, *112*, 7146.

(136) Zeng, H. J.; Khuu, T.; Chambreau, S. D.; Boatz, J. A.; Vaghjiani, G. L.; Johnson, M. A. Ionic Liquid Clusters Generated from Electrospray Thrusters: Cold Ion Spectroscopic Signatures of Size-Dependent Acid−Base Interactions. *J. Phys. Chem. A* **2020**, *124*, 10507−10516.

(137) Brüssel, M.; Brehm, M.; Pensado, A. S.; Malberg, F.; Ramzan, M.; Stark, A.; Kirchner, B. On the ideality of binary mixtures of ionic liquids. *Phys. Chem. Chem. Phys.* **2012**, *14*, 13204−13215.

(138) Fumino, K.; Bonsa, A.-M.; Golub, B.; Paschek, D.; Ludwig, R. Non-Ideal Mixing Behaviour of Hydrogen Bonding in Mixtures of Protic Ionic Liquids. *ChemPhysChem* **2015**, *16*, 299−304.

(139) Matthews, R. P.; Villar-Garcia, I. J.; Weber, C. C.; Griffith, J.; Cameron, F.; Hallett, J. P.; Hunt, P. A.; Welton, T. A structural investigation of ionic liquid mixtures. *Phys. Chem. Chem. Phys.* **2016**, *18*, 8608−8624.

(140) Sessa, F.; D'Angelo, P.; Migliorati, V. Combined distribution functions: A powerful tool to identify cation coordination geometries in liquid systems. *Chem. Phys. Lett.* **2018**, *691*, 437−443.

(141) Jeffrey, G. A. *An Introduction to Hydrogen Bonding*; Oxford University Press, 1997.

(142) Hayes, R.; Imberti, S.; Warr, G. G.; Atkin, R. The Nature of Hydrogen Bonding in Protic Ionic Liquids. *Angew. Chem., Int. Ed.* **2013**, *52*, 4623−4627.

(143) Skarmoutsos, I.; Welton, T.; Hunt, P. A. The importance of timescale for hydrogen bonding in imidazolium chloride ionic liquids. *Phys. Chem. Chem. Phys.* **2014**, *16*, 3675−3685.

(144) Luzar, A. Resolving the hydrogen bond dynamics conundrum. *J. Chem. Phys.* **2000**, *113*, 10663−10675.

(145) Gehrke, S.; von Domaros, M.; Clark, R.; Hollóczki, O.; Brehm, M.; Welton, T.; Luzar, A.; Kirchner, B. Structure and lifetimes in ionic liquids and their mixtures. *Faraday Discuss.* **2018**, *206*, 219−245.

(146) Roy, D.; Patel, N.; Conte, S.; Maroncelli, M. Dynamics in an Idealized Ionic Liquid Model. *J. Phys. Chem. B* **2010**, *114*, 8410−8424.

(147) Zhang, W.; van Duin, A. C. T. ReaxFF Reactive Molecular Dynamics Simulation of Functionalized Poly(phenylene oxide) Anion Exchange Membrane. *J. Phys. Chem. C* **2015**, *119*, 27727−27736.

(148) Dasgupta, N.; Kyung Shin, Y.; Fedkin, M. V.; van Duin, A. C. T. ReaxFF molecular dynamics simulations on the structure and dynamics of electrolyte water systems at ambient temperature. *Comput. Mater. Sci.* **2020**, *172*, 109349.

(149) Borner, A.; Li, Z.; Levin, D. A. Prediction of Fundamental Properties of Ionic Liquid Electrospray Thrusters using Molecular Dynamics. *J. Phys. Chem. B* **2013**, *117*, 6768−6781.

(150) Zhang, F.; Jiang, X.; Chen, G.; He, Y.; Hu, G.; Qiao, R. Electric-Field-Driven Ion Emission from the Free Surface of Room Temperature Ionic Liquids. *J. Phys. Chem. Lett.* **2021**, *12*, 711−716.

(151) Zhang, J.; Zhang, K.; Wang, W.; Shahzad, A.; Cheng, Y.; Cai, G. Permeation by Electrowetting Actuation: Revealing the Prospect of a Micro-valve Based on Ionic Liquid. *J. Colloid Interface Sci.* **2022**, *608*, 114−119.

(152) Enomoto, T.; Parmar, S. M.; Yamada, R.; Wirz, R. E.; Takao, Y. Molecular Dynamics Simulations of Ion Extraction from Nano-droplets for Ionic Liquid Electrospray Thrusters. *J. Electr. Propul.* **2022**, *1*, 13.

(153) Senftle, T. P.; Hong, S.; Islam, M. M.; Kylasa, S. B.; Zheng, Y.; Shin, Y. K.; Junkermeier, C.; Engel-Herbert, R.; Janik, M. J.; Aktulga, H. M.; Verstraelen, T.; Grama, A.; van Duin, A. C. T. The ReaxFF reactive force-field: development, applications and future directions. *npj Comput. Mater.* **2016**, *2*, 15011.

(154) Lee, H.; Litzinger, T. A. Chemical kinetic study of HAN decomposition. *Combust. Flame* **2003**, *135*, 151−169.

(155) Pasini, A.; Torre, L.; Romeo, L.; Cervone, A.; D'Agostino, L. Reduced-Order Model for H2O2 Catalytic Reactor Performance Analysis. *J. Propul. Power* **2010**, *26*, 446−453.

(156) Sun, S.; Ouyang, R.; Zhang, B.; Zhang, T.-Y. Data-driven discovery of formulas by symbolic regression. *MRS Bull.* **2019**, *44*, 559−564.

(157) Kerr, D. Sensitivity Analysis and Uncertainty Quantification in Reduced-Order Monopropellant Catalyst Bed Model. Ph.D. Thesis, University of California, Los Angeles, 2019.

(158) Ferguson, R. E.; Esparza, A. A.; Chambreau, S. D.; Vaghjiani, G. L.; Shafirovich, E. Studies on the Combustion of HAN/Methanol/ Water Propellants and Decomposition of HAN and HEHN. *Int. J. Energ. Mater. Chem. Propul.* **2021**, *20*, 21−31.

(159) Alavi, S.; Thompson, D. L. Hydrogen bonding and proton transfer in small hydroxylammonium nitrate clusters: A theoretical study. *J. Chem. Phys.* **2003**, *119*, 4274−4282.

(160) Aquino, A. J. A.; Tunega, D.; Haberhauer, G.; Gerzabek, M. H.; Lischka, H. Solvent Effects on Hydrogen Bonds: A Theoretical Study. *J. Phys. Chem. A* **2002**, *106*, 1862−1871.

(161) Zhou, W.; Liu, J.; Chambreau, S. D.; Vaghjiani, G. L. Formation and fragmentation of 2-hydroxyethylhydrazinium nitrate (HEHN) cluster ions: a combined electrospray ionization mass spectrometry, molecular dynamics and reaction potential surface study. *Phys. Chem. Chem. Phys.* **2023**, *25*, 17370−17384.